TIME-DEPENDENT IONIZATION IN DYNAMIC SOLAR AND STELLAR ATMOSPHERES. I. METHODS

W. RAMMACHER[1] AND P. ULMSCHNEIDER

Institut für Theoretische Astrophysik, Universität Heidelberg, Tiergartenstrasse 15, D-69121 Heidelberg, Germany; ulm@ita.uni-heidelberg.de

ABSTRACT

We propose a new numerical method to compute one-dimensional time-dependent wave propagation in stellar atmospheres that incorporates the time-dependent treatment of hydrogen ionization together with an evaluation of radiation losses under departures from local thermodynamic equilibrium (NLTE). The method permits us to calculate acoustic waves and longitudinal magnetohydrodynamic (MHD) tube waves. We have tested the method for the solar atmosphere by calculating the propagation of three types of waves, namely, a monochromatic acoustic wave, a stochastic acoustic wave, and a stochastic longitudinal tube wave. It was found that with a time-dependent treatment of the hydrogen ionization (as well as the Mg ionizations) the degree of ionization (H^+/H) and the Mg II/Mg ratio become insensitive to the temperature fluctuations, even in the presence of weak and moderately strong shocks. Only when strong shocks appear do the transition rates become large enough to cause a high correlation between the degree of ionization and the high post-shock temperatures. Our calculations show that a mean degree of ionization gets established that increases with height and is very little perturbed by the local temperature fluctuations of the wave. In stochastic calculations, strong shocks appeared periodically (roughly every 3 minutes), which in their postshock regions carried a zone of high or complete ionization. Tests with different numbers of frequency and height points, as well as of the rate of convergence of the Λ-iteration, were performed.

Subject headings: atomic processes — hydrodynamics — MHD — stars: atmospheres — Sun: atmosphere — waves

1. INTRODUCTION

Kneer & Nakagawa (1976) for the Sun and Klein, Stein, & Kalkofen (1976) for an A0 main-sequence star were among the first to attempt acoustic wave calculations where the time-dependent ionization of hydrogen and the treatment of radiation under departures from local thermodynamic equilibrium (NLTE) were consistently treated. The fact that the ionization of hydrogen does not instantly adjust to the hot postshock temperature after a shock has traversed a chromospheric gas element was pointed out by Kneer (1980), who found that the relaxation time for the ionization of hydrogen varies from about 100 s in the middle solar chromosphere to about 1000 s in the upper chromosphere.

In the following decade not much had been done to implement this in chromospheric wave calculations (see, e.g., Herbold et al. 1985; Ulmschneider, Muchmore, & Kalkofen 1987; Rammacher & Ulmschneider 1992) because these computations were concerned with the physics of the lower and middle chromosphere where hydrogen is only very little ionized. However, with the intense interest in the time behavior of the Ca II H and K line profiles and in the cross-correlations between the Doppler shift fluctuations of the Ca II infrared triplet (IRT) lines, with the sights set on explaining the onset of the transition layer to the corona, it was felt absolutely essential to include the correct time-dependent treatment of hydrogen ionization into an acoustic wave code (Carlsson & Stein 1992, 1994, 1997, 2002; Skartlien, Carlsson, & Stein 1994; Hansteen 1993).

Carlsson & Stein (1992) found that when including the ionization of hydrogen in the energy conservation equation used in the wave computation and assuming local thermodynamic equilibrium (LTE), most of the wave energy goes into the hydrogen ionization and very little into heating. This situation is very different when one considers NLTE and computes the hydrogen ionization with time-dependent rate equations. Here the radiative transition rates delay the ionization, which leads to a much stronger chromospheric temperature rise. Using an empirical acoustic spectrum from observations of a low-lying Fe line as input in their wave calculations, Carlsson & Stein (1994, 1997) were able to find reasonable agreement with the observed Ca II H line profile variations, which are caused by isolated strong shocks that roughly periodically (with a period around 3 minutes) propagate through the outer solar atmosphere. In addition, these calculations showed essentially zero phase shifts between the velocity fluctuations in the Ca II IRT lines, a phenomenon that is attributed to the fact that these lines are generated in the same hot postshock layer (Skartlien et al. 1994). This corrected the suggestion by Fleck & Deubner (1989) that the zero phase shift phenomenon ought to be explained by standing waves.

While the simulations of Carlsson & Stein (1994, 1997) agree in an overall manner with the observed Ca II H line profile variations, there has also been much discussion about some significant discrepancies (Kalkofen 2001; Kalkofen, Ulmschneider, & Avrett 1999; Kalkofen & Ulmschneider 1999). Although these authors agree with Carlsson & Stein (1994, 1997) that the H line profile variations are probably caused by acoustic shocks, they point out that the simulated H line cores appear to be too deep by about an order of magnitude and that the intensities of the blue peaks are too high by roughly an order of magnitude. In addition, Kalkofen

[1] Visiting Scientist, Center for Space Plasma and Aeronomic Research (CSPAR), University of Alabama in Huntsville, Huntsville, AL 35899.

(2003) pointed out that in reality acoustic waves propagate as spherical waves or at least in a cone. He warns that therefore the plane-parallel wave computations of Carlsson & Stein (1994, 1997) appear to be highly idealized if not inappropriate and the strong solitary shock picture might be an artifact of the plane wave computation.

That plane wave calculations with an acoustic wave spectrum invariably lead to strong shocks with a 3 minute–type wave period is also found in our present work and attributed to the overtaking of shocks. We confirm the strong shocks found in the computations of Carlsson & Stein (1994, 1997). However, recent observations by Wunnenberg, Kneer, & Hirzberger (2002) show that the acoustic energy generation is nonuniformly distributed over the solar surface, a fact that was already suggested long ago by Kuperus (1972). In a realistic situation, therefore, one has a large number of acoustic sources at discrete locations distributed all over the solar surface from which spherically or conically propagating acoustic waves emanate. As pointed out by Ulmschneider (2003), such waves will intersect at oblique angles and cannot produce shock overtakings. Therefore, plane wave computations with shock overtakings are a poor representation of the mechanical heating mechanism of the chromosphere. If plane wave computations cannot be avoided as a result of the present lack of computational power to fully simulate a three-dimensional situation with multiple discrete acoustic sources, then Ulmschneider (2003) suggests that the use of monochromatic waves might be the next best choice because they produce the weak shock heating but do not generate shock overtakings.

However, the discussion of the structure and modeling of the solar chromosphere is not the topic of the present paper. Our present work aims to describe a method for treating the full time dependence of the hydrogen ionization, which is an essential feature of any hydrodynamic and magnetohydrodynamic (MHD) wave simulation. Our present plane wave computations should be taken as test calculations to illustrate the method and explain its consequences and therefore should not be seen as proposed theoretical chromosphere models. In their recent work, Carlsson & Stein (2002) discussed the time behavior of the hydrogen ionization in more detail. These authors showed that the strong shocks in their computations generated a mean degree of hydrogen ionization that continuously increases with height. They also found that the relaxation times responsible for the delayed ionization and recombination are quite large, in the order of 10^3–10^5 s, and therefore much longer than typical fluctuations in the acoustic wave, but that behind strong shocks these relaxation times became very small.

The fact that noninstantaneous ionization processes are essential for the explanation of chromospheric phenomena has also been found by analyzing observations. Judge, Carlsson, & Wilhelm (1997) suggested that anomalous behavior of He I $\lambda584$ may result from long ionization/ recombination timescales. That nonequilibrium ionization will severely alter the properties of C II emission lines has been predicted by Judge & Carpenter (1998). Moreover, Carlsson, Judge, & Wilhelm (1997) pointed out that the whole foundation for using spectral features in static models to infer physical properties in the chromosphere such as the Ca II emission or the CO absorption must be called into question.

In this paper (the first of a series) we discuss a complete revision of our time-dependent plane-parallel acoustic and MHD wave code, which is based on the method of charac-

teristics and which by treating shocks as discontinuities allows the computation of a large number of shocks (Ulmschneider et al. 1977, 1987; Ulmschneider & Kalkofen 1978; Herbold et al. 1985; Cuntz & Ulmschneider 1988; Cuntz 1990; Rammacher & Ulmschneider 1992; Fawzy et al. 2002). We now treat the hydrogen ionization in a fully time-dependent manner by solving the statistical rate equations. This treatment at first is for a three-level hydrogen atomic model (two bound levels and the continuum) in which the computation of the Lyα line is simplified using an escape probability method. We also treat the ionization of the first three ionization stages of Mg in a fully time-dependent manner. The details of the treatments of elements other than hydrogen, such as Mg, Ca, and C, will be given in W. Rammacher (2003a, in preparation, hereafter Paper II). The analytical results on relaxation times are going to be presented in W. Rammacher (2003b, in preparation, hereafter Paper III).

Our present paper is organized as follows. In § 2 we summarize the basic hydrodynamic and MHD equations and discuss the shock treatment, the boundary and initial conditions, the treatment of the NLTE radiative transfer, and the treatment of the time-dependent statistical rate equations. Four different wave calculations were performed and described in § 3 together with various tests of the accuracy and convergence of the method. Our conclusions are given in § 4. Appendix A describes the particle conservation equations, the time-dependent rate equations, and the thermodynamic derivatives, while Appendix B outlines the polynomial solution for determining the electron density. In Appendix C we discuss the generalization of our method to an N-level atomic model of hydrogen.

2. HYDRODYNAMIC AND MAGNETOHYDRODYNAMIC EQUATIONS

2.1. Acoustic Waves

A continuous one-dimensional flow is described by the following hydrodynamic equations in the Euler (laboratory) frame, namely, the continuity equation, momentum equation, and energy equation (e.g., Zeldovich & Raizer 1967; Landau & Lifshitz 1959):

$$A\frac{\partial \rho}{\partial t} + \frac{\partial \rho u A}{\partial x} = 0 \,, \qquad (1)$$

$$\rho\left(\frac{\partial u}{\partial t} + u\frac{\partial u}{\partial x}\right) + \frac{\partial p}{\partial x} + \rho g(x) = 0 \,, \qquad (2)$$

$$\frac{\partial S}{\partial t} + u\frac{\partial S}{\partial x} = \frac{dS}{dt}\bigg|_{\mathrm{rad}} \,, \qquad (3)$$

where, as functions of Euler height x and time t, ρ is the density, u is the gas velocity, p is the gas pressure, $g(x)$ is the gravity, and S is the specific entropy; $dS/dt|_{\mathrm{rad}}$ is the radiative heating function that describes the net increase of entropy in the gas by absorption of photons. These equations are valid for spherical flows where $A(x)$ is the area, while for flows in a tube, $A(x)$ is the tube cross section. For plane-parallel geometry equation (1) is replaced by taking $A = 1$, $dA/dx = 0$, and by using constant gravity $g(x) = g_0$.

We assume that the physical state can be described by the velocity u and two thermodynamic variables T and p, where T is the kinetic temperature. In order to solve the above set of equations, we use the method of characteristics that rewrites the three partial differential equations (1)–(3) into a set of six ordinary differential equations. Following, e.g., Ulmschneider et al. (1977) or Cuntz & Ulmschneider (1988), the following set of compatibility relations can be derived:

$$du \pm \frac{1}{\rho c_S} dp$$
$$+ \left[\mp c_S \rho \left(\frac{\partial T}{\partial p} \right)_S \frac{dS}{dt} \bigg|_{\text{rad}} \pm c_S u \frac{1}{A} \frac{dA}{dx} + g(x) \right] dt = 0 , \quad (4)$$

valid along the C^+ and C^- characteristics given by

$$\frac{dx}{dt} = u \pm c_S , \quad (5)$$

where the top sign is for the C^+ and the bottom sign for the C^- characteristic, and

$$dS = \frac{dS}{dt} \bigg|_{\text{rad}} dt , \quad (6)$$

which can be written

$$dT - \left(\frac{\partial T}{\partial p} \right)_S dp - \left(\frac{\partial T}{\partial S} \right)_p \frac{dS}{dt} \bigg|_{\text{rad}} dt = 0 , \quad (7)$$

valid along the fluid path, the characteristic C^0 given by

$$\frac{dx}{dt} = u . \quad (8)$$

These equations are written in the Euler (x, t) frame, and in order to write the thermodynamic relations and thermodynamic derivatives in terms of T and p, they must be augmented by the particle conservation equations, which in the case of time-dependent ionization of hydrogen requires the solution of the time-dependent rate equations along the fluid path. The calculation of the density ρ, the adiabatic sound speed c_S, and $(\partial T/\partial S)_p$ and $(\partial T/\partial p)_S$ is discussed in § 2.6 and Appendix A.

In the Lagrange (a, t) frame the Lagrange height $a = x(t = 0)$ marks mass elements in the initial atmosphere that has an initial density distribution $\rho_0(a)$ and an initial tube cross section $A_0(a)$. Mass conservation requires that

$$\left(\frac{\partial x}{\partial a} \right)_t = \frac{\rho_0 A_0}{\rho A} , \quad (9)$$

and the transformation equations between the Euler and Lagrange frames are given by

$$\left(\frac{\partial}{\partial a} \right)_t = \frac{\rho_0 A_0}{\rho A} \left(\frac{\partial}{\partial x} \right)_t , \quad \left(\frac{\partial}{\partial t} \right)_a = \left(\frac{\partial}{\partial t} \right)_x + u \left(\frac{\partial}{\partial x} \right)_t . \quad (10)$$

The local gas velocity is defined by

$$u = \left(\frac{\partial x}{\partial t} \right)_a . \quad (11)$$

Since the density in the element changes because its upper and lower boundaries move with different speed or because the area varies, the continuity equation in the Lagrange frame can be written as

$$\left(\frac{\partial \rho}{\partial t} \right)_a + \frac{\rho^2 A}{\rho_0 A_0} \left(\frac{\partial u}{\partial a} \right)_t + \frac{\rho u}{A} \frac{dA}{dx} = 0 . \quad (12)$$

In addition, one has the momentum and energy conservation equations

$$\left(\frac{\partial u}{\partial t} \right)_a + \frac{A}{\rho_0 A_0} \left(\frac{\partial p}{\partial a} \right)_t + g(x) = 0 , \quad (13)$$

$$\left(\frac{\partial S}{\partial t} \right)_a = \frac{dS}{dt} \bigg|_{\text{rad}} . \quad (14)$$

Equations (12)–(14) in the Lagrange frame correspond to equations (1)–(3) in the Euler frame. They can be brought in characteristic form and provide the same two compatibility relations given by equation (4) along the C^+ and C^- characteristics. However, these two characteristics in the Lagrange frame are now given by

$$\frac{da}{dt} = \pm c_S \frac{\rho A}{\rho_0 A_0} . \quad (15)$$

From equation (14) we get the compatibility relation given by equation (6) along the fluid path characteristic C^0, which is now given by $a = \text{const}$. Our code is able to use both the Euler and Lagrange frames.

2.2. Longitudinal Tube Waves

To describe longitudinal MHD tube waves that propagate in vertically directed magnetic flux tubes in a stellar atmosphere, we use the thin flux tube approximation. The equations (Herbold et al. 1985; Fawzy, Ulmschneider, & Cuntz 1998; Fawzy et al. 2002) for continuous one-dimensional flows are then given in the Euler frame by

$$\frac{\partial \rho A}{\partial t} + \frac{\partial \rho u A}{\partial x} = 0 , \quad (16)$$

$$\frac{\partial u}{\partial t} + u \frac{\partial u}{\partial x} + \frac{1}{\rho} \frac{\partial p}{\partial x} + g(x) = 0 , \quad (17)$$

$$\frac{\partial S}{\partial t} + u \frac{\partial S}{\partial x} = \frac{dS}{dt} \bigg|_{\text{rad}} , \quad (18)$$

$$\Phi = AB = \text{const} , \quad (19)$$

$$B^2 = 8\pi(p_e - p) . \quad (20)$$

Here p and p_e are the gas pressures inside and outside the tube, respectively, and B is the magnetic field strength. In addition, the cross section A is now also time-dependent, which allows breathing (distensibility; see Lighthill 1978, p. 93) of the tube. Equations (16)–(18) correspond to equations (1)–(3) for acoustic waves, while equations (19) and (20) represent the conservation of the magnetic flux Φ and the horizontal pressure balance between inside and outside the tube. All quantities are considered to be both functions of height x and time t except for p_e. Because of the thin flux tube approximation, we assume that the external pressure is not perturbed by the wave in the tube and therefore $p_e = p_e(x)$ is independent of time.

Similarly as for the acoustic wave case, the system of equations can be transformed into characteristic form. With

the Alfvén speed

$$c_A = \sqrt{\frac{B^2}{4\pi\rho}} \qquad (21)$$

and tube speed c_T given by

$$\frac{1}{c_T^2} = \frac{1}{c_S^2} + \frac{1}{c_A^2} , \qquad (22)$$

the following compatibility relations are found:

$$du \pm \frac{1}{\rho c_T} dp \mp \left[c_T \rho \left(\frac{\partial T}{\partial p} \right) \frac{dS}{dt} + \frac{c_T u}{c_A^2 \rho} \frac{dp_e}{dx} \mp g(x) \right] dt = 0 , \qquad (23)$$

along the two C^+ and C^- characteristics given by

$$\frac{dx}{dt} = u \pm c_T , \qquad (24)$$

plus identical equations as equations (6)–(8). In the Lagrange frame equation (16) is replaced by

$$A \left(\frac{\partial \rho}{\partial t} \right)_a + \rho \left(\frac{\partial A}{\partial t} \right)_a + \frac{\rho^2 A^2}{\rho_0 A_0} \left(\frac{\partial u}{\partial a} \right)_t = 0 , \qquad (25)$$

which reduces to equation (12) if the time dependence of A is dropped and the term $(\partial A/\partial t)|_a$ is transformed using equation (10). The Lagrange equations corresponding to equations (17) and (18) are the same as equations (13) and (14). They can be transformed into the same compatibility relations given by equation (23) along the C^+ and C^- characteristics given in the Lagrange frame by

$$\frac{da}{dt} = \pm c_T \frac{\rho A}{\rho_0 A_0} , \qquad (26)$$

whereas for acoustic waves, one has equation (6) along the fluid path characteristic C^0 given by $a = $ const.

2.3. *Shocks and Rankine-Hugoniot Relations*

In the method of characteristics, hydrodynamic and MHD shocks are treated as discontinuities that interrupt the regions of continuous flows. Here we follow earlier work of Ulmschneider et al. (1977), Herbold et al. (1985), and Cuntz & Ulmschneider (1988). At the shock we solve the Rankine-Hugoniot relations, which represent the conservation of mass, momentum, and energy flows across the discontinuity. Using parameters a and b, the Rankine-Hugoniot relations can be written as

$$\rho_1 v_1 A_1 = \rho_2 v_2 A_2 , \qquad (27)$$

$$A_1 \left(\rho_1 v_1^2 - a + b p_1 \right) = A_2 \left(\rho_2 v_2^2 - a + b p_2 \right) , \qquad (28)$$

$$\frac{1}{2} v_1^2 + E_1 + \frac{p_1}{\rho_1} = \frac{1}{2} v_2^2 + E_2 + \frac{p_2}{\rho_2} , \qquad (29)$$

with

$$v_1 = u_1 - U_{sh} , \qquad (30)$$

$$v_2 = u_2 - U_{sh} , \qquad (31)$$

where v_1 and v_2 are the flow velocities in the shock frame moving with the shock and U_{sh} is the shock speed. Here ρ_1, ρ_2 are the densities, u_1, u_2 are the flow velocities, A_1, A_2 are the tube cross sections, p_1, p_2 are the gas pressures, and E_1, E_2 are the internal energies in front of and behind the shock, respectively.

For acoustic waves one has $a = 0$, $b = 1$, and $A_1 = A_2 = 1$ in plane-parallel, spherical or tube geometry. For longitudinal tube waves (Herbold et al. 1985) we have $a = 2p_e$, $b = 2$, and from horizontal pressure balance together with magnetic flux conservation the relationships

$$A_1 = \frac{\phi}{\sqrt{8\pi(p_e - p_1)}} , \quad A_2 = \frac{\phi}{\sqrt{8\pi(p_e - p_2)}} . \qquad (32)$$

To solve for the shock position at the new time level and to determine the physical variables in front of and behind the shock discontinuity, we have to determine 15 unknowns. These are E_1, ρ_1, p_1, T_1, A_1, v_1, u_1, E_2, ρ_2, p_2, T_2, A_2, v_2, u_2, and U_{sh}. For these unknowns we have exactly 15 relations, namely, the four equations given by equations (30)–(32); the four thermodynamic relations $\rho_1 = \rho_1(p_1, T_1)$, $\rho_2 = \rho_2(p_2, T_2)$, $E_1 = E_1(p_1, T_1)$, $E_2 = E_2(p_2, T_2)$; the three Rankine-Hugoniot relations given by equations (27)–(29); and four compatibility relations along four characteristics. The latter is because the shock runs faster than any disturbances propagating with sound speed (or tube speed) in front of the shock; one thus has three characteristics (C^+, C^0, C^-) in front of the shock, and as the sound speed (or tube speed) behind the shock is greater than the shock speed, we have one (C^+) characteristic behind the shock path (e.g., Ulmschneider et al. 1977).

For a rapid solution we eliminate unknowns as far as possible. We first eliminate the shock speed U_{sh} by using equations (27), (30), and (31) and find

$$U_{sh} = \frac{u_1 \rho_1 A_1 - u_2 \rho_2 A_2}{\rho_1 A_1 - \rho_2 A_2} . \qquad (33)$$

Note that in the special case of weak shocks, equation (33) is numerically unstable because of $\rho_1 A_1 \simeq \rho_2 A_2$. In this case, U_{sh} needs to be calculated using well-known weak shock formulae available for acoustic waves (Ulmschneider 1970) and longitudinal tube waves (Cuntz 1999). Second, from equations (27), (28), (30), and (31) we derive a quadratic equation for the postshock density ρ_2,

$$k_1 \rho_2^2 + k_2 \rho_2 + k_3 = 0 , \qquad (34)$$

with

$$k_1 = A_2^2 \left[\rho_1 A_1 (u_2 - u_1)^2 + a(A_2 - A_1) + b(p_1 A_1 - p_2 A_2) \right] , \qquad (35)$$

$$k_2 = -A_2 \rho_1 A_1 \left[\rho_1 A_1 (u_2 - u_1)^2 + 2a(A_2 - A_1) + 2b(p_1 A_1 - p_2 A_2) \right] , \qquad (36)$$

$$k_3 = A_1^2 \rho_1^2 [a(A_2 - A_1) + b(p_1 A_1 - p_2 A_2)] . \qquad (37)$$

This equation has two solutions,

$$\rho_2 = \frac{\rho_1 A_1}{A_2} \frac{k}{\rho_1 A_1 (u_2 - u_1)^2 + k} , \quad \rho_2 = \frac{\rho_1 A_1}{A_2} , \qquad (38)$$

with

$$k = a(A_2 - A_1) + b(p_1 A_1 - p_2 A_2) . \qquad (39)$$

The second solution is irrelevant as it represents the trivial

case $u_2 = u_1$ as seen from equations (27), (30), and (31). In addition, we use the energy conservation in the form

$$E_2(p_2, T_2) - E_1 + (u_1 - u_2)U_{\text{sh}} + \frac{1}{2}\left(u_2^2 - u_1^2\right) + \frac{p_2}{\rho_2} - \frac{p_1}{\rho_1} = 0 \ . \tag{40}$$

The procedure of determining the 15 unknowns at the new shock point is now as follows. We first assume a new value U_{sh}. With this the shock position at the new time level can be calculated. Using the three front-shock characteristics and the thermodynamic routines, the values E_1, ρ_1, p_1, T_1, A_1, v_1, and u_1 are then determined. Now a value u_2 is assumed that allows using equations (32), (33), and (38) to write equation (40) as a function $f(p_2, T_2) = 0$, which together with the thermodynamic relation $\rho_2 = \rho_2(p_2, T_2)$ provides two equations for the two unknowns p_2 and T_2, which are solved with a Newton-Raphson iteration. This gives new estimates for U_{sh}, v_2, A_2, and E_2. Finally, the C^+ characteristic behind the shock provides a new estimate for u_2. With these new values U_{sh} and u_2 the entire procedure is repeated until convergence.

The thermodynamic relations depend on the number densities of the particles (atoms, ions, electrons), which are provided as solutions of the time-dependent rate equations (§ 2.6). At the shock discontinuity, where we have a jump in the physical variables, we assume that this jump occurs so rapidly that the ratios between the bound level populations and the degree of ionization are identical on both sides of the shock. With enough points in the postshock region, care is taken that the level populations and degree of ionization can subsequently adjust to the jump of the kinetic temperature.

2.4. Initial and Boundary Conditions

For our wave calculations we need initial atmosphere models into which the waves propagate. Starting from such an initial atmosphere, our aim is that the wave code after minimal computation time generate a final state where the atmosphere together with the wave has come to dynamical equilibrium, where major velocity and temperature fluctuations, as well as strong shocks resulting from the onset of our calculation, have left the computational domain. Only in such a situation is it possible to study the introduced wave independently of these so-called switch-on effects. To minimize switch-on effects, we start with radiative and hydrostatic equilibrium models constructed by specifying the stellar parameters effective temperature T_{eff} and gravity g. These models are generated using temperature correction methods (Cuntz, Rammacher, & Ulmschneider 1994) to ensure that the specified total radiation flux σT_{eff}^4 is correctly reproduced. Here identical emitters of radiation as in the wave code are employed. It has to be noted, however, that because of the absence of mechanical heating, these initial atmosphere models are quite unrealistic. This is due to the low radiative equilibrium temperatures, which lead to small-scale heights by which the mass is initially concentrated near the bottom of the atmosphere. To achieve a realistic mass distribution over height, wave heating must act for a considerable time, until the dynamical equilibrium state is reached.

For MHD wave computations, magnetic flux tube models are subsequently embedded in this external atmosphere by specifying a magnetic field strength B and a tube diameter d (usually equal to the scale height) at the stellar surface. The shape of the flux tube is determined by magnetic flux conservation and horizontal pressure balance. After first spreading exponentially, the tube at greater height attains a constant cross section determined by the assumed magnetic filling factor f, when the magnetic field fills out the entire available space (f is the ratio of the area covered by magnetic fields divided by the total surface area of the star). To achieve constant cross section at great height, the external gas pressure is assumed to be augmented by magnetic pressure from neighboring tubes. For details see, e.g., Fawzy et al. (1998, 2002). The temperature in the flux tube is again determined by employing temperature correction methods. It is typically close to the external temperature.

At the bottom boundary of such models the wave is introduced by assuming a piston boundary condition. For monochromatic waves the piston velocity is prescribed by

$$u(0, \ t) = -u_{00} \sin \frac{2\pi}{P} t \ , \tag{41}$$

where u_{00} is the wave amplitude, P is the period, and t is the time. For acoustic waves the wave amplitude is given by

$$u_{00} = \sqrt{\frac{2F_A}{c_0 \rho_0}} \ , \tag{42}$$

where F_A is the initial wave energy flux, ρ_0 is the density, and c_0 is the sound speed at the bottom boundary. For longitudinal tube waves, these equations hold if F_A is replaced by the longitudinal wave flux F_L and c_0 by the tube speed c_{T0}. The minus sign in equation (41) is taken to minimize switch-on effects at the start of the wave computation.

For acoustic frequency spectra the piston velocity is prescribed by $N \approx 100$ partial waves

$$u(0, \ t) = \sum_{n=0}^{N} u_n \sin(\omega_n t + \varphi_n) \ , \tag{43}$$

where u_n are the amplitudes of the partial waves, ω_n are the chosen frequencies from the partial wave spectrum, and φ_n are arbitrary but constant phase angles. The wave amplitudes are directly related to the selected turbulent energy spectrum and to the total wave energy fluxes F_A or F_L. For details see Sutmann, Musielak, & Ulmschneider (1998) and Fawzy et al. (2002).

Acoustic wave energy generation calculations to specify F_A and the acoustic wave spectrum on the basis of the Lighthill-Stein theory for a wide range of late-type stars with various T_{eff}, g, and metallicities were performed by Ulmschneider, Theurer, & Musielak (1996) and Ulmschneider et al. (1999). In addition, using magnetic tube models as described above, longitudinal wave energy fluxes F_L and wave spectra were calculated using an analytical approach by Musielak, Rosner, & Ulmschneider (1989, 2000, 2002) and Musielak et al. (1995) and a numerical approach by Ulmschneider & Musielak (1998) and Ulmschneider, Musielak, & Fawzy (2001).

The mentioned bottom boundary conditions are strictly valid only for the Lagrange frame where the piston represents the lowest mass element in the atmosphere. Here the specification of the velocity replaces the information from the missing C^+ characteristic arriving from below the

computational domain (Ulmschneider et al. 1977). In the Euler frame it is correct to take one boundary condition when the fluid path (C^0 characteristic) is in the computational domain. However, if this is not the case, two boundary conditions must be specified. Since the piston motion at the lowest grid point is small, one can extrapolate this second boundary condition (e.g., the temperature) from the two next internal grid points, which can lead to secular motions of the piston in monochromatic wave computations but does not cause problems in a stochastic wave calculation. A better solution is to follow Theurer (1998) and use a previous run of a wave calculation conducted over a very short computational domain in the Lagrange frame and then interpolate the two boundary conditions at the lowest grid point for the Euler calculation. In the case of supersonic inflows even more variables have to be specified as boundary conditions (see, e.g., Cuntz & Ulmschneider 1988). As mentioned above, our wave code allows computations in both the Euler and the Lagrange frames.

Other boundary conditions must be specified at the top of the atmosphere. Here the situation is in principle similar to the lower boundary, except that we cannot prescribe a piston velocity. Instead, following Ulmschneider et al. (1977) and Ulmschneider (1986), a transmitting boundary condition is employed by specifying the velocity in accordance to the behavior of simple waves.

2.5. *Treatment of Radiative Transfer*

In our wave computations knowledge of radiation fields of lines and continua is required for two reasons, to evaluate the radiative heating function $dS/dt|_{rad}$ in the energy equation (3) and to compute the radiative absorption and emission rates in the statistical rate equations to determine the populations of the energy levels and the electron density. As the ratios of the number densities are essentially the source functions of the radiative transfer equations, a consistent time-dependent computation of the radiation fields is complicated.

To accurately evaluate the radiative heating function for a given wave phase, a large number of photospheric and chromospheric emitters, lines, and continua of the most abundant elements would have to be computed. Such an approach is not reasonable for a time-dependent wave calculation as it would require excessive amounts of computer time. This is because a typical wave calculation requires the height distribution of the radiative heating rates for about 100,000 wave phases. Therefore, an approximation that provides both reasonable speed and accuracy is required. This we attempt by concentrating on a few emitters. These are the H^- and Lyman continua as well as the Mg II k and Ca II K lines, where the line losses are scaled upward to represent the total chromospheric radiative losses and gains.

For the treatment of the H^- contribution we follow Ulmschneider & Kalkofen (1978) (employing a precomputed electron density table as a function of T and p), while the Mg II k and Ca II K lines were treated in a two-level atom approximation according to Ulmschneider et al. (1987) using line data of Kalkofen, Ulmschneider, & Schmitz (1984). In all cases we solve the radiative transfer equations and the statistical equilibrium equations for the NLTE populations. Different from previous work, however, we treat the ionizations of Mg I to Mg II and Mg II to Mg III as well as the similar Ca ionizations in a time-dependent manner (for

details see Paper II). Because the energies of the first and second ionization stages of these elements are smaller than (or comparable to) the Balmer and Lyman edge energies, respectively, we use the mean intensities of the Balmer and Lyman continua as the dominating radiation fields for the calculation of the radiative rate integrals. This implies that we first compute the hydrogen ionization and then treat the other elements for which the electron densities are then known. For these Mg and Ca ionization calculations we use three-level atomic models consisting only of the ground levels of the first three ionization stages. Ionization treatments for additional elements such as C are also implemented (see Paper II). We assume that the treatment of the Mg II and Ca II lines using a two-level atomic model and employing the statistical equilibrium equations is appropriate because the bound-bound transitions are orders of magnitude faster than the bound-continuum transitions.

The correct treatment of the radiative losses in the chromospheric emission lines necessitates the use of partial redistribution (PRD) because the line wings are formed by coherent scattering and only the line cores contribute to the radiative energy loss. However, a line treatment implementing PRD (Ulmschneider 1994) leads to excessive computation times that cannot be tolerated in time-dependent wave calculations. We thus follow Hünerth & Ulmschneider (1995) by employing so-called pseudo-PRD, which computes the line assuming complete frequency redistribution (CRD) but artificially removes the damping wings from the lines by multiplying the damping parameter a in the Voigt function by a factor of $1/100$. Simulations of solar Mg II line cooling with full PRD show that pseudo-PRD works very well (Hünerth & Ulmschneider 1995).

The total chromospheric radiation losses are simulated by multiplying our Mg II pseudo-PRD k line computation by a factor of 2 to also account for the Mg II h line and the similar Ca II K line computation by a factor of 5 to take into account the H line and the three IRT lines. We found that the Fe II emission can also be crudely taken into account by simply doubling the Ca II losses. In our computations we therefore multiply the Ca II K line pseudo-PRD losses by a factor of 10. For the computations of the single lines we use a revised operator splitting method (Buchholz et al. 1994), which allows for the proper handling of shocks. We use 19 frequency points for H^- and 29 frequency points each for the two lines. For the exploratory test calculations in the present paper we use an even simpler approach and follow our previous work (e.g., Buchholz, Ulmschneider, & Cuntz 1998), replacing the Ca and Mg line losses by computing only the Mg II k line with CRD and without further scaling. The overestimation made by using ordinary CRD (instead of pseudo-PRD) amounts roughly to the total chromospheric line radiation losses.

The computation of the Lyman and Balmer continua of hydrogen must be specially discussed as these continua are required for the radiative rates in our treatment of time-dependent ionization of hydrogen. The Lyman continuum is also important for time-dependent ionization effects of Mg and Ca. In cases in which the flow speed is orders of magnitude smaller than the speed of light the radiative transfer equation for these continua reads

$$\mu \frac{\partial I_\nu}{\partial \tau_\nu} = I_\nu - S_\nu \, , \qquad (44)$$

where $I_\nu = I(\mu, x, \nu)$ is the specific intensity, $S_\nu = S(x, \nu)$ is the source function, ν is the frequency, μ is the angle cosine, and $\tau_\nu = \tau(x, \nu)$ is the optical depth. Neglecting stimulated emission the Lyman continuum source function is given by

$$S_{\nu \mathrm{Ly}} = \frac{B_\nu}{b_1} = B_\nu \frac{n_1^*}{n_3^*} \frac{n_3}{n_1}, \qquad (45)$$

where $b_1 = n_1 n_3^* / n_1^* n_3$ is the departure coefficient for the ground level. For the Balmer continuum, one has

$$S_{\nu \mathrm{Ba}} = \frac{B_\nu}{b_2} = B_\nu \frac{n_2^*}{n_3^*} \frac{n_3}{n_2}, \qquad (46)$$

where $b_2 = n_2 n_3^* / n_2^* n_3$ is the departure coefficient for the second level. Here B_ν is the Planck function while n_1, n_2, and n_3 are the number densities for the ground level, second level, and continuum level of hydrogen, respectively, whereas the quantities with asterisks denote LTE number densities (see eqs. [70]–[72]). In our present work we take an atomic model of hydrogen that consists of only these three levels.

The transfer equation can be solved using the integral formalism of Kalkofen & Ulmschneider (1984). With the depth index i, running from inside to outside, the intensities I^+ and I^- can be expressed as follows:

$$I_\nu^+(i) = aI_\nu^+(i-1) + bS_\nu(i) + cS_\nu(i-1), \qquad (47)$$
$$I_\nu^-(i) = aI_\nu^-(i+1) + bS_\nu(i) + cS_\nu(i+1), \qquad (48)$$

with

$$a = \frac{2-\delta}{2+\delta}, \quad b = c = \frac{\delta}{2+\delta}, \quad \text{if } \delta \leq 1, \qquad (49)$$
$$a = c = \frac{1}{2\delta+1}, \quad b = \frac{2\delta-1}{2\delta+1}, \quad \text{if } \delta > 1, \qquad (50)$$

where δ is the optical depth between neighboring grid points. It can be seen that equations (47) and (48) with given source functions allow us to compute the unknown Lyman and Balmer continuum intensities that would permit us to calculate the radiative absorption and emission rates (eqs. [65]–[68]), while with given intensities, the solution of the time-dependent rate equations would allow us to compute the populations and with it the source functions. As unfortunately both intensities and source functions are unknown, one has two possibilities: either to attempt a complete linearization of the problem in terms of the level populations (Carlsson 1986) or to apply a Λ-iteration.

The Λ-iteration assumes an arbitrary initial source function, for instance, from the last time step of the wave computation, and calculates the intensity, from which an improved source function is computed, etc. It is well known that this iteration has poor convergence (e.g., Buchholz et al. 1994), yet in our case this iteration was found to converge rapidly (see § 3.7). This is very likely due to the long relaxation times for all ionization and recombination processes in the chromosphere by which the change of the radiation field in time and space is only small and works essentially as a "rarefaction" of the optically thick Lyman continuum. In optically thin cases the Λ-iteration is known to converge rapidly. Small relaxation times in the chromosphere are confined to the post-shock regions of strong shocks (see also Carlsson & Stein

2002). In these cases, rapid ionization takes place and again leads locally to an optically thin Lyman continuum.

The great advantage of using the Λ-iteration is computational speed (see Figs. 8 and 9) by which, e.g., 100,000 iterations can be executed in a few seconds of computer time. A similar procedure as for the Lyman continuum can be used for the computation of the Balmer continuum. However, it was found to be a good approximation to compute the radiative rates using a Planck function with a radiation temperature T_{rad} (see § 2.6).

2.6. Time-dependent Rate Equations

In a wave calculation with time-dependent ionization we have to solve the statistical rate equations. Considering radiative processes R and collisional processes C and assuming that the hydrogen atom consists of $N = 3$ levels, namely, two bound levels plus the continuum level, the population for level i is given by

$$\frac{\partial n_i}{\partial t} + \frac{\partial n_i u}{\partial x} = \sum_{i \neq j}^{N} (n_j P_{ji} - n_i P_{ij}), \qquad (51)$$

where P_{lk} denotes the rate of transitions (per cm^3 and s) taking place from level l to level k and $P_{lk} = R_{lk} + C_{lk}$. This equation is the usual conservation equation for the particle density n_i, except that one now has to consider also creations and destructions due to transitions from and to other levels. Therefore, the left-hand side of equation (51) would be zero if the particles of species i were conserved. Here the first term on the left-hand side of equation (51) gives the change of n_i with time, while the second term gives the change of n_i, which occurs because at the top boundary of a volume element a different particle flux leaves the element than enters at the bottom boundary. As a result of transitions from and to other levels, however, particles n_i can also be created (first term on the right-hand side) or destroyed (second term on the right-hand side).

Mass conservation in the Lagrange frame after equation (25) reads

$$\left(\frac{\partial \rho}{\partial t}\right)_a + \frac{\rho}{A}\left(\frac{\partial A}{\partial t}\right)_a + \frac{\rho^2 A}{\rho_0 A_0}\left(\frac{\partial u}{\partial a}\right)_t = 0. \qquad (52)$$

As we want to use p and T as independent thermodynamic variables, we write

$$\begin{aligned} \left(\frac{\partial \rho}{\partial t}\right)_a &= \left(\frac{\partial \rho}{\partial p}\right)_S \left(\frac{\partial p}{\partial t}\right)_a + \left(\frac{\partial \rho}{\partial S}\right)_p \left(\frac{\partial S}{\partial t}\right)_a \\ &= \frac{1}{c_S^2}\left(\frac{\partial p}{\partial t}\right)_a - \rho^2 \left(\frac{\partial T}{\partial p}\right)_S \frac{dS}{dt}\bigg|_{\mathrm{rad}}, \end{aligned} \qquad (53)$$

where we have used equations (A16), (A19), and (14). Introducing equation (53) in equation (52) and dividing by ρ gives

$$\frac{\rho A}{\rho_0 A_0}\left(\frac{\partial u}{\partial a}\right)_t = -\frac{1}{\rho c_S^2}\left(\frac{\partial p}{\partial t}\right)_a + \rho\left(\frac{\partial T}{\partial p}\right)_S \frac{dS}{dt}\bigg|_{\mathrm{rad}} - \frac{1}{A}\left(\frac{\partial A}{\partial t}\right)_a. \qquad (54)$$

Now the left-hand side of equation (51) in the Lagrange

frame can be written as

$$\left(\frac{\partial n_i}{\partial t}\right)_a + \frac{n_i}{A}\left(\frac{\partial A}{\partial t}\right)_a + \frac{n_i \rho A}{\rho_0 A_0}\left(\frac{\partial u}{\partial a}\right)_t , \qquad (55)$$

which with help from equation (54) reads

$$\left(\frac{\partial n_i}{\partial t}\right)_a - n_i\left[\frac{1}{\rho c_S^2}\left(\frac{\partial p}{\partial t}\right)_a - \rho\left(\frac{\partial T}{\partial p}\right)_S \frac{dS}{dt}\bigg|_{\mathrm{rad}}\right] . \qquad (56)$$

Defining the advection term

$$W = \rho\left(\frac{\partial T}{\partial p}\right)\frac{dS}{dt}\bigg|_{\mathrm{rad}} - \frac{1}{\rho c_S^2}\frac{dp}{dt} , \qquad (57)$$

we therefore get for the populations of our three levels, where $n_3 = n_{\mathrm{H}^+}$ and where $(\partial n_i/\partial t)|_a$ is written in the more usual form dn_i/dt,

$$\begin{aligned}\frac{dn_1}{dt} = &\, n_2(R_{21} + C_{21}) + n_3(R_{31} + C_{31}) \\ &- n_1(R_{12} + C_{12} + R_{13} + C_{13}) - n_1 W , \qquad (58)\end{aligned}$$

$$\begin{aligned}\frac{dn_2}{dt} = &\, n_1(R_{12} + C_{12}) + n_3(R_{32} + C_{32}) \\ &- n_2(R_{21} + C_{21} + R_{23} + C_{23}) - n_2 W , \qquad (59)\end{aligned}$$

$$\begin{aligned}\frac{dn_3}{dt} = &\, n_1(R_{13} + C_{13}) + n_2(R_{23} + C_{23}) \\ &- n_3(R_{31} + C_{31} + R_{32} + C_{32}) - n_3 W . \qquad (60)\end{aligned}$$

In addition, we have total particle conservation (see eq. [A6]),

$$(n_1 + n_2 + n_3)\frac{1 + z_{\mathrm{el}}}{X_{\mathrm{el}}} + n_3 = \frac{p}{kT} = n_{\mathrm{tot}} , \qquad (61)$$

where n_{tot} is the total particle density, and the conservation of electrons (see eq. [A5]),

$$n_e = n_3 + (n_1 + n_2 + n_3)\frac{Z_{\mathrm{el}}}{X_{\mathrm{el}}} . \qquad (62)$$

X_{el} and Z_{el} are the element abundances of hydrogen and the metals, respectively (for details see Appendix A).

Equations (58)–(62) represent five equations for the four unknowns n_1, n_2, n_3, and n_e. In calculations with time-independent ionization (for which $W = 0$ and $dn_i/dt = 0$) usually the rate equation for level 3 is dropped; however, in our case with time-dependent ionization we find it numerically advantageous (to avoid the occasional appearance of unrealistic negative populations) to retain the three rate equations and at first drop the particle conservation equation. The numerical solution of the rate equations (plus the conservation equation for n_e) leads to a result that closely approaches total particle conservation. We subsequently enforce particle conservation to computer accuracy by applying a small correction using

$$n_{i(\mathrm{corr})} = n_i \frac{n_{\mathrm{tot}}}{\sum_i n_i} . \qquad (63)$$

These corrections have an average relative error in the range 10^{-4} to 10^{-5}. The main sources of the errors are the computations of the numerical derivatives needed for the calculation of the thermodynamic quantities (see Appendix A). The use of equation (63) ensures perfect particle

conservation and does not change the ratios of the occupation numbers.

Before we explain how to solve equations (58)–(62), we must discuss the radiation and collisional rates in more detail. As in the present work we are not interested in the details of the Lyα line, we treat it using an escape probability method given by

$$n_2 R_{21} - n_1 R_{12} = n_2 A_{21}\frac{1}{1 + \tau_{\mathrm{Ly\alpha}}} , \qquad (64)$$

where $\tau_{\mathrm{Ly\alpha}}$ is the Lyα optical depth. For the Lyman and Balmer continuum, we have

$$R_{13} = \frac{1}{2}\int_{-1}^{+1}\int_{\nu_1}^{\infty}\frac{4\pi}{h\nu}\alpha_{13}I_{\nu\mu}\,d\nu\,d\mu , \qquad (65)$$

$$R_{31} = \frac{1}{2}\frac{n_1^*}{n_3^*}\int_{-1}^{+1}\int_{\nu_1}^{\infty}\frac{4\pi}{h\nu}\alpha_{13}\left(\frac{2h\nu^3}{c^2} + I_{\nu\mu}\right)e^{-h\nu/kT}\,d\nu\,d\mu , \qquad (66)$$

where h is the Planck constant, c is the light speed, and μ is the angle cosine, and

$$R_{23} = \frac{1}{2}\int_{-1}^{+1}\int_{\nu_2}^{\infty}\frac{4\pi}{h\nu}\alpha_{23}I_{\nu\mu}\,d\nu\,d\mu , \qquad (67)$$

$$R_{32} = \frac{1}{2}\frac{n_2^*}{n_3^*}\int_{-1}^{+1}\int_{\nu_2}^{\infty}\frac{4\pi}{h\nu}\alpha_{23}\left(\frac{2h\nu^3}{c^2} + I_{\nu\mu}\right)e^{-h\nu/kT}\,d\nu\,d\mu , \qquad (68)$$

respectively. Here α_{13} and α_{23} are the Lyman and Balmer radiative cross sections and ν_1 and ν_2 are the Lyman and Balmer ionization frequencies, respectively. The starred number densities indicate the number densities under LTE conditions (see eqs. [70] and [71]). In our present work the Balmer continuum is treated employing a radiation temperature $T_{\mathrm{rad}} = 5400$ K (Noyes & Kalkofen 1970) assuming $I_\nu = B_\nu(T_{\mathrm{rad}})$ with

$$B_\nu(T) = \frac{2h\nu^3}{c^2}\frac{1}{e^{h\nu/kT} - 1} . \qquad (69)$$

For the radiation temperature in the Balmer continuum Ayres (1975) gave a handy estimate $T_{\mathrm{rad}} = \epsilon T_{\mathrm{eff}}$ with ϵ between 0.72 and 0.88 that depends only weakly on the stellar spectral type and luminosity class.

For later use, we also define $\tilde{R}_{31} = R_{31}/n_e$ and $\tilde{R}_{32} = R_{32}/n_e$. Note that $\tilde{R}_{31}$ and $\tilde{R}_{32}$ depend only on radiative quantities and the temperature, but not on the electron density, which is also the case for R_{13} and R_{23}. The Saha and Boltzmann factors are given by

$$\frac{n_1^*}{n_3^*} = n_e\left(\frac{h^2}{2\pi m_e kT}\right)^{3/2}e^{E_1/kT} , \qquad (70)$$

$$\frac{n_2^*}{n_3^*} = 4n_e\left(\frac{h^2}{2\pi m_e kT}\right)^{3/2}e^{E_2/kT} , \qquad (71)$$

$$\frac{n_2^*}{n_1^*} = 4e^{-E_{12}/kT} , \qquad (72)$$

where $E_1 = E_{\mathrm{H}}$, $E_2 = \frac{1}{4}E_{\mathrm{H}}$, and $E_{12} = \frac{3}{4}E_{\mathrm{H}}$. For the

collisional rates we find

$$C_{13} = n_e \Omega_1 e^{-E_H/kT} , \quad C_{31} = \frac{n_1^*}{n_3^*} C_{13} , \quad (73)$$

$$C_{23} = n_e \Omega_2 e^{-E_H/4kT} , \quad C_{32} = \frac{n_2^*}{n_3^*} C_{23} , \quad (74)$$

$$C_{12} = n_e \Omega_{21} e^{-E_{12}/kT} , \quad C_{21} = \frac{n_1^*}{n_2^*} C_{12} = n_e \frac{1}{4} \Omega_{21} . \quad (75)$$

The Ω-values are collisional cross sections, which slowly vary with temperature T. Following Vernazza, Avrett, & Loeser (1981; see their eqs. [3] and [4] and Table 7), Ω_1, Ω_2, and Ω_{21} can be approximated by $\Omega_1 = 3.92 \times 10^{-9}$, $\Omega_2 = 7.59 \times 10^{-8}$, and $\Omega_{21} = 2.38 \times 10^{-8}$ taking the values at $T = 9000$ K. It is also possible to take into account the weak temperature dependence of the Ω-values by using

$$\Omega_1 = 5.465 \times 10^{-11} \sqrt{T} (0.3 \log T - 0.435) , \quad (76)$$

$$\Omega_2 = 5.465 \times 10^{-11} \sqrt{T} \left(\frac{5.444 \times 10^7}{T^2} - \frac{2.8186 \times 10^4}{T} \right.$$
$$\left. + 19.987 - 5.891 \times 10^{-5} T \right) , \quad (77)$$

$$\Omega_{21} = 5.465$$
$$\times 10^{-11} \sqrt{T} \left(-30.206 + 3.861 \log T + \frac{305.64}{\log^2 T} \right) , \quad (78)$$

following Percival (1966) for Ω_1 and Ω_2 and Burke, Ormonde, & Whittaker (1967) for Ω_{21}. In chromospheric models of solar-type stars, the temperature dependence of the Ω-values is usually found to be negligible considering that usually the radiative rates dominate the collisional rates by several orders of magnitude.

We now use equations (58)–(62) for the determination of the four unknowns n_1, n_2, n_3, and n_e. As a result of the dependence of some of the rates on the electron density, we get a nonlinear system of equations. Because a simultaneous iterative solution for all four unknowns is sometimes numerically unstable (occurrence of negative occupation numbers and electron densities), we reduce the equation system analytically as far as possible. For the purpose of integrating equations (58)–(60) along the fluid path, these equations must be written as difference equations. As an example, the rate equation for the ground (first) level reads

$$\frac{n_{1P} - n_{1T}}{\Delta t} = \frac{1}{2} [n_{2P} P_{21P} + n_{3P} P_{31P} - n_{1P}(P_{12P} + P_{13P} + W_P)]$$
$$+ \frac{1}{2} [n_{2T} P_{21T} + n_{3T} P_{31T}$$
$$- n_{1T}(P_{12T} + P_{13T} + W_T)] , \quad (79)$$

with similar equations for the second and third level. The subscripts P and T denote the values at the actual time level (for which we seek the solution) and at the old time level, respectively. Note that the points T and P mark the start and end points of the fluid path over the time interval Δt as described by the C^0 characteristic (eq. [8]). Note that different from the Lagrange frame, in a Eulerian frame these points are not at the same height.

In a first step, we solve formally the resulting linear system of equations for n_1, n_2, n_3, disregarding the fact that n_e is unknown (see eqs. [B8]–[B10]). We then separate the coefficients of this system in terms with and without n_e. The formal solutions for the n_i depend now only on n_e and known parameters such as temperature, pressure, transition rates, etc. Introducing the formal solutions in equation (62), we get finally a polynomial of fifth order:

$$v_5 n_e^5 + v_4 n_e^4 + v_3 n_e^3 + v_2 n_e^2 + v_1 n_e + v_0 = 0 . \quad (80)$$

Details of this calculation and the polynomial coefficients are found in Appendix B. Since equation (80) is of fifth order, five different solutions for n_e are obtained. However, it is always found that only one physical solution exists with n_e in the interval $[0, n_{\rm tot}]$. All other mathematical solutions for n_e are negative, larger than $n_{\rm tot}$, or conjugate complex. With n_e known, the occupation numbers n_i can then be calculated by resubstitution. In a last step we apply equation (63) to enforce perfect particle conservation. In our code equation (80) is used a large number of times and its solution using Newton-Raphson iteration is very fast and stable.

Finally, let us address the question of how equation (80) would change if we increased the number of bound levels and consider an N-level atom with $N - 1$ bound levels plus the continuum level. It is easy to show (see Appendix C) that we would then have a polynomial of order $N + 2$. This is in agreement with equation (80), where we have a fifth-order polynomial for a two bound level plus continuum atomic model.

3. TRIAL CALCULATIONS AND TESTS

3.1. *General Remarks*

To show first results based on our method, we perform several acoustic wave calculations in the solar atmosphere, both monochromatic waves and waves with an acoustic frequency spectrum. Here we do not attempt to model solar situations but concentrate on working out the fundamental difference between a fully time-dependent ionization treatment solving the statistical rate equations and a time-independent NLTE treatment that solves only the statistical equilibrium equations. In order to demonstrate that our fully time-dependent ionization treatment can also be employed for magnetic wave propagation, we show the results of a longitudinal tube wave calculation with a longitudinal wave spectrum.

These calculations allow us to show the basic properties of fully time-dependent ionization in outer stellar atmospheres. As discussed above, we use a simple hydrogen atomic model and represent the chromospheric radiation losses assuming, in addition to H^- continuum losses, Mg II k line losses in CRD. This leads to a rather fast code, which allows us to compute a wave with 256 height points (plus eight shock points) stretching over 2360 km, with 5000 time steps over 0.5 hr of real time, in about 3 hr of computer time on a 1.3 GHz desktop PC, and a memory requirement of less than 128 MB. To use a more elaborate radiation treatment with Mg II k and Ca II K line losses, the computation time would increase only by about a factor of 1.2.

In a second series of calculations we perform several tests. For the initial atmosphere model we have constructed a radiative equilibrium solar model with $T_{\rm eff} = 5770$ K and
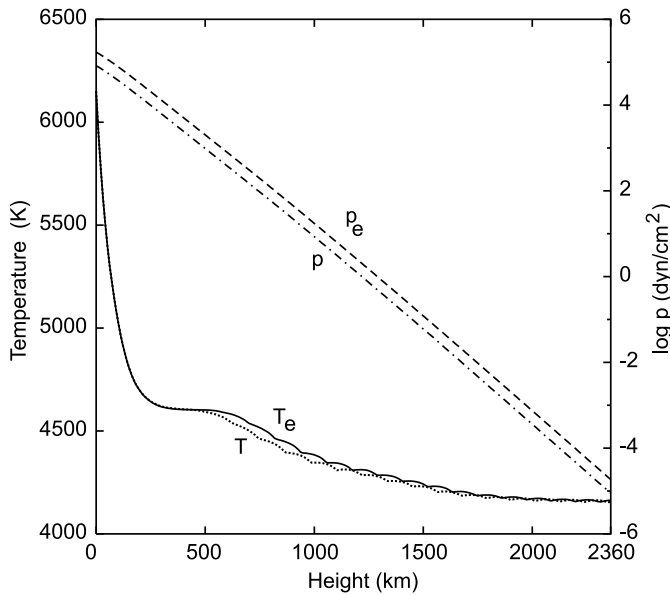
FIG. 1.—Initial radiative equilibrium solar atmosphere model. T_e and p_e indicate temperature and pressure in the external atmosphere, while T and p are temperature and pressure inside a magnetic flux tube embedded in the external atmosphere.

gravity $g = 2.736 \times 10^4$ cm s^{-2} using Population I–type solar metal abundances. For our magnetic wave calculations we have embedded a magnetic flux tube in this atmosphere model that at the solar surface has a field strength of $B = 1500$ G and a tube diameter of 130 km. As discussed above, the tube first spreads exponentially and at about 1000 km height reaches a constant diameter of 390 km. Figure 1 shows the temperatures (T_e, T) and gas pressures (p_e, p) of these external atmosphere and tube models.

3.2. Acoustic Waves

Figures 2a–2c show three phases of a monochromatic sinusoidal wave with period $P = 60$ s and initial acoustic flux $F_A = 1 \times 10^8$ ergs cm^{-2} s^{-1}, which has been introduced into the initial atmosphere by employing a piston. Here the fully time-dependent hydrogen ionization treatment has been implemented, as well as the fully time-dependent treatment of the Mg ionizations (discussed in more detail in Paper II). It can be seen that as a result of the rapid decrease of the atmospheric density with height, the temperature amplitude grows rapidly with height and at around 600 km leads to shock formation. These shocks then quickly attain a sawtooth shape. In Figure 2a the topmost shock is particularly strong as it runs into the low-density undisturbed atmosphere. At the later phases (Figs. 2b and 2c) it is seen that the wave amplitude decreases when the calculation approaches a state of dynamical equilibrium where the temperature jumps at the shocks attain a limiting strength, which is a well-known property of monochromatic waves in stellar atmospheres.

Also shown in the three figures is the Mg II/Mg fraction (with Mg = Mg I + Mg II + Mg III). We find that except for the high-temperature region near the bottom of the atmosphere, Mg is largely in the singly ionized state. At later times (Fig. 2c) it is seen that there is a slight buildup of Mg III similarly to what happens to H$^+$.

The behavior of the hydrogen ionization (H$^+$/H) in Figure 2a is surprising. From the topmost strong shock near 2200 km, with a 10,000 K temperature jump, we would have expected an instant ionization of the medium. It can be seen, however, that it produces only weak ionization and that the next much weaker shock near 1300 km with a temperature jump of only 6000 K leads to a higher degree of ionization, although the degree of ionization behind both shocks is tiny. About 140 s later (Fig. 2b) the degree of ionization has much increased, but again it is seen that it apparently does not react much to the local temperature fluctuation. There is no instant jump of the degree of ionization behind the strong shock near 2300 km. Moreover, at the greatest height, H$^+$/H has still not reacted to the several strong shocks that approached and have been transmitted at the top boundary. Apparently, the gas reacts only very slowly to the shock temperatures and the reaction (relaxation) time increases with height together with the rapid density decrease of the atmosphere. This behavior of the radiative relaxation time that depends on the density is discussed in more detail in Paper III of this series. It is in good agreement with the results of Kneer (1980) and Carlsson & Stein (2002).

In Figure 2c, after about twice the time of Figure 2b, a steady state has been established, where the degree of ionization appears to settle into a permanent outwardly increasing mean H$^+$/H distribution, over which small superposed fluctuations associated with the temperature fluctuations of the wave propagate. This permanent mean degree of hydrogen ionization is similar to the permanent mean Mg III/Mg distribution discussed above.

It is interesting to compare these results now with a wave calculation with similar period and acoustic flux where, however, the hydrogen ionization is treated in a time-independent manner, that is, by solving only the statistical equilibrium equations instead of the time-dependent rate equations. These calculations are shown in Figures 2d–2f. We have selected similar wave phases as in Figures 2a–2c to allow for easy comparison. Comparing Figures 2a and 2d shows the very different behavior of the time-independent treatment. Here indeed it is seen, what one would have naively expected, that the degree of ionization is intimately correlated with the temperature fluctuation. Behind the shocks the high postshock temperatures instantly raise the degree of ionization. Moreover, the strongest shock generates the highest degree of ionization. But also in front of the shocks does one get a high degree of ionization. This is due to the generated intense Lyman continuum radiation that ionizes hydrogen in the cold regions in front of the shocks. This is particularly apparent for the topmost shock, in front of which the Lyman continuum optical depth is very small. Such a precursor radiation has also been found in the work of Klein et al. (1976).

Figures 2e and 2f further confirm this behavior. Here because of the buildup of the mean chromospheric temperature, a stronger reaction of H$^+$/H to the temperature jump at the shock is found. In Figure 2f a dynamical equilibrium is reached. A similar behavior is seen in the distribution of the Mg II/Mg fraction where the ionization to Mg III is also strongly correlated with the temperature.

Monochromatic waves are well behaved numerically and quickly lead to a dynamical steady state with a limiting shock strength behavior in stellar atmospheres, yet these waves simulate only poorly the violent fluctuations in real stellar atmospheres that come about when the propagation
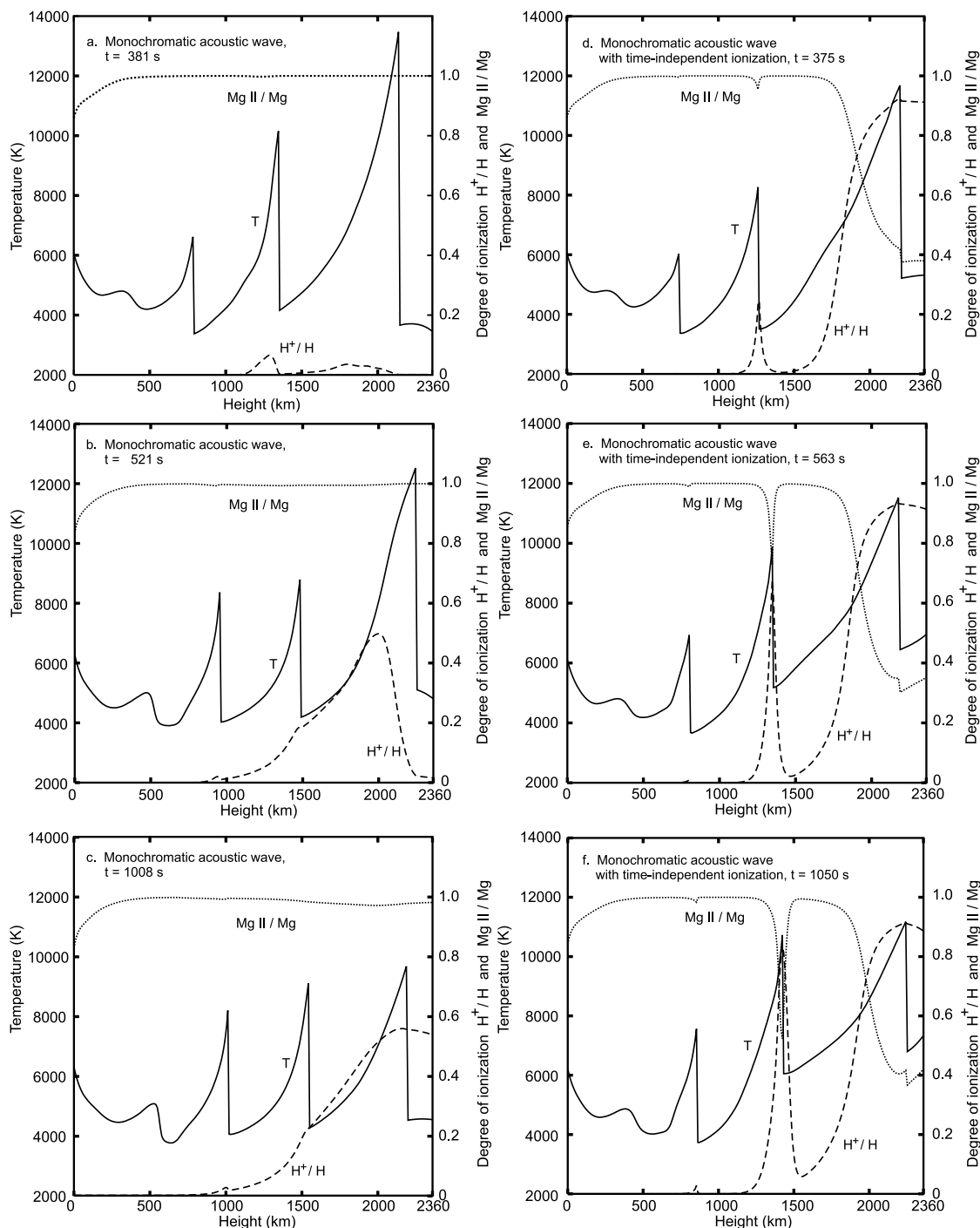
Fig. 2.—Wave phases of monochromatic acoustic waves at indicated times, calculated with different treatments of the hydrogen and Mg ionizations. *Left:* Computations with fully time-dependent ionization. *Right:* calculations with a time-independent ionization treatment. Displayed are temperatures T, as well as Mg II/Mg and H^+/H fractions, vs. Euler height.

of acoustic wave spectra is considered. Here the phenomenon of shocks overtaking one another comes into play, which creates strong shocks. These shocks in the solar atmosphere excite 3 minute–type atmospheric resonances, which in turn influence the shock overtaking process (see also Rammacher & Ulmschneider 1992).

For our calculation of an acoustic wave with an acoustic spectrum (based on the eKmG turbulent energy spectrum of Musielak et al. 1994) we assumed the same initial acoustic energy flux $F_A = 1 \times 10^8$ ergs cm^{-2} s^{-1} as

for our monochromatic calculations. Figures 3a–3c show three phases of a stochastic wave computation using such a spectrum. These phases were selected so that they can be compared to the phases of Figure 2. Note that the ordinate scale is 3 times larger. Compared to the monochromatic calculation, it is seen that the shocks in the stochastic wave calculation occur in a rather irregular manner and that very strong shocks appear. This phenomenon is in good agreement with the results of Carlsson & Stein (1994, 1997). The strong shock in
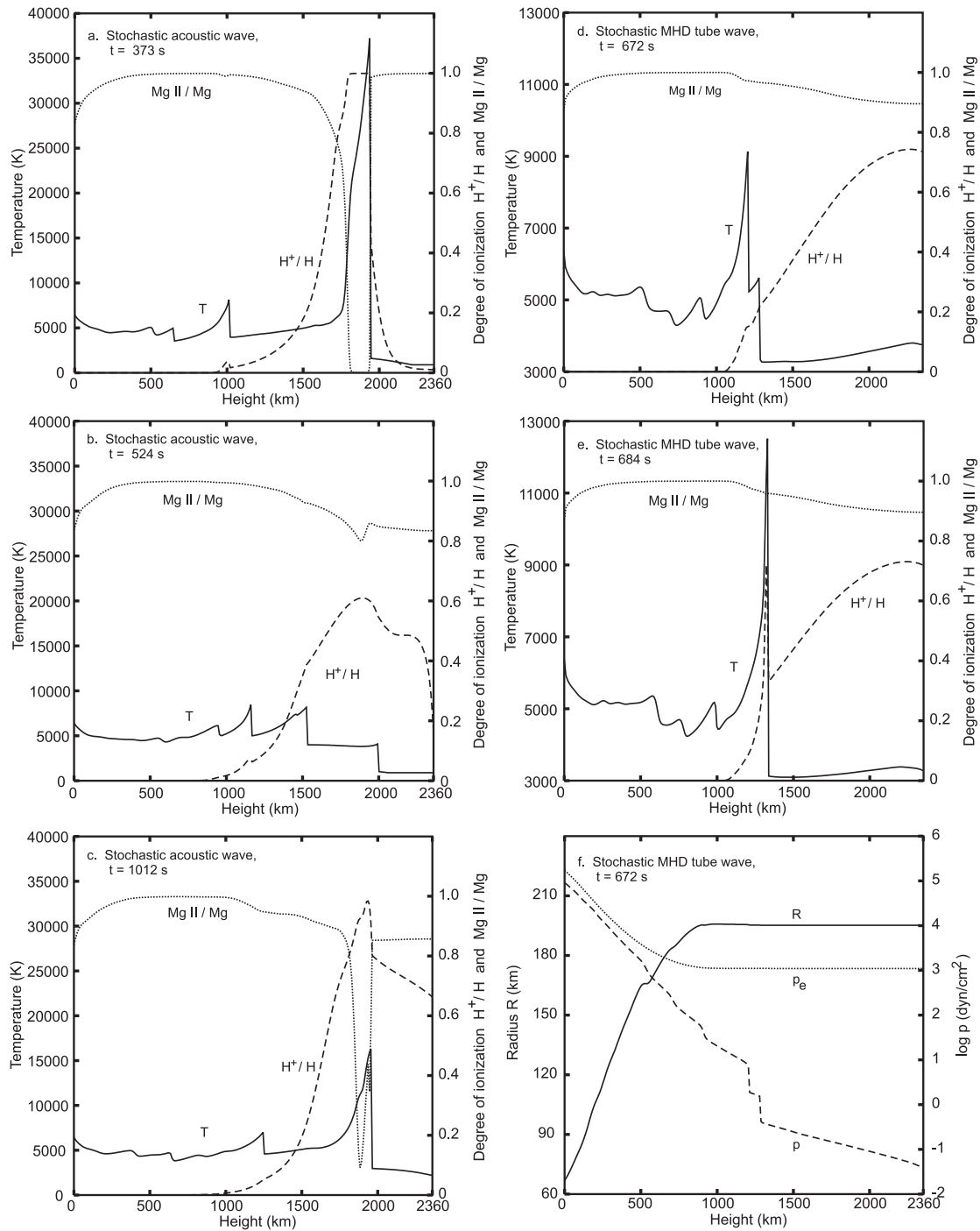
Fig. 3.—Wave phases of stochastic acoustic and longitudinal magnetic waves at indicated times, calculated with fully time-dependent hydrogen and Mg ionizations. *Left:* Acoustic wave. *Right:* Longitudinal magnetic tube wave. Displayed are temperatures T, as well as Mg II/Mg and H^+/H fractions, vs. Euler height. Panel f shows the radius and the external and internal gas pressures in the magnetic flux tube for the wave phase displayed in panel d.

Figure 3a pushes a lot of mass over the top boundary (in this Euler frame calculation) so that adiabatic expansion generates a cool region in the top 1000 km of the model over which the wave propagates. There are also numerous smaller shocks as seen, e.g., in Figure 3b, which have strengths similar to those of the monochromatic wave. Shock overtaking in Figure 3c has created another strong shock with a more than 10,000 K temperature jump. Such shocks occur in our stochastic wave calculation roughly every 3 minutes.

Compared to Figure 2a, the strong shock in Figure 3a at a similar time shows a very different behavior in the degree of ionization. Note that this is also seen in the Mg III/Mg fraction. While H^+/H in Figure 2a is only little affected, there is a fully ionized hydrogen region behind the strong shock, despite the fact that Figures 3a–3c display a fully time-dependent ionization calculation. This different behavior is due to the much larger temperature jump where now the temperature-sensitive collisional ionization rates dominate the ionization. When the temperature jumps are

smaller, the radiative rates dominate the collisional rates by many orders of magnitude, which leads to the slow reaction to the temperature fluctuation seen in Figure 2. However, a dominant collisional ionization rate leads to an instant effect on the degree of ionization similar to the situation in a time-independent calculation. A similar reaction of H^+/H to a strong shock is seen in Figure 3c, which in this case is mainly caused by high radiative rates.

Note also that the strong Lyman continuum precursor radiation from the strong shocks causes extended ionization in front of the shocks as seen in Figures 3a and 3c. Again as in the monochromatic calculation, a permanent outwardly rising distribution of ionized hydrogen gets established (best seen in Fig. 3b, where the H ionization is comparable to that in Fig. 2b), which is perturbed by superimposed effects from the strong shocks but on average shows a higher degree of ionization than in the monochromatic case. The same behavior as in the hydrogen ionization is also seen in the Mg II/Mg fraction. It can be seen in Figure 3a that behind the strong shock Mg II is completely ionized to Mg III and that after the shock near 2000 km in Figure 3c both the Mg III/Mg fraction and H^+/H take time to build up behind the shock.

3.3. Magnetic Waves

Figures 3d–3f show a longitudinal MHD tube wave calculation with initial energy flux $F_L = 1 \times 10^8$ ergs cm^{-2} s^{-1} and an acoustic spectrum for which we take again the eKmG turbulent energy spectrum of Musielak et al. (1994) as a basis. Comparison of Figures 3d and 3b shows that, in principle, the magnetic wave has a similar behavior as the acoustic wave. It is seen that a permanent outwardly rising H^+/H distribution develops, which is mirrored in the behavior of the Mg II/Mg fraction, and leads to a similar buildup of an outwardly rising Mg III/Mg distribution.

Figures 3d and 3e show two wave phases that are close in time and demonstrate the effect of shock overtaking on the degree of ionization. While in Figure 3d the degree of ionization is little affected by the two 2000 and 4000 K temperature jumps in these weak and moderate-strength shocks, this is different when the shocks merge into a strong shock with a 10,000 K temperature jump. The high temperature of the strong shock, through the transition rates, affects the degree of ionization in the same way as found in the stochastic acoustic wave calculation. In summary, Figures 3d and 3e show the two basic types of hydrogen ionization processes occurring when frequency spectra are employed: (1) slow ionization processes in the upper chromosphere for shocks of weak or moderate strength and (2) fast ionization processes for the strong shocks formed by shock overtaking in the stochastic flow field. The effects of the wave on the geometry of the flux tube are shown in Figure 3f. It is seen that the tube radius is breathing with the wave; that is, there are radius excursions of the wave superposed over the exponentially spreading tube geometry, which at a height of about 1000 km reaches a constant radius as a result of the crowding by neighboring flux tubes. Also seen are the pressure jumps associated with the shocks. Aside from this different radius behavior, the longitudinal MHD tube wave and the acoustic wave are very similar.
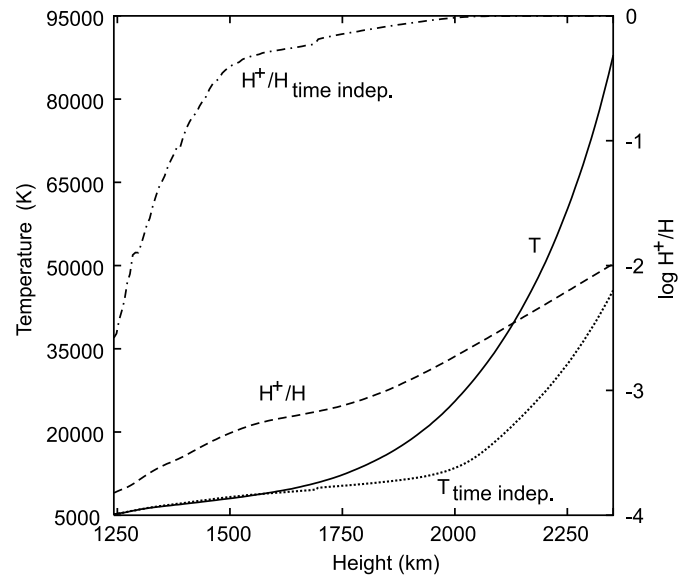
FIG. 4.—Temperatures and degrees of hydrogen ionization in the hot postshock region of the first shock entering the initial undisturbed atmosphere for the two wave calculations of Fig. 2.

3.4. Individual Shock Behavior

So far we have concentrated on how the degree of hydrogen and Mg ionizations changes as a result of the different types of treatments of the ionization. However, there is also a direct influence on other physical variables of the wave depending on whether we treat the ionization in a time-dependent or time-independent manner. This influence is demonstrated in Figure 4, where we have plotted the development of the first shock over height, which enters the undisturbed initial atmosphere for our monochromatic acoustic wave calculations. This first shock is very strong, and Figure 4 shows the postshock temperatures and the degree of ionization of the two calculations of Figure 2. As already discussed above, it is seen that the degree of ionization remains small in the case with time-dependent hydrogen ionization while it is large in the time-independent case.

Initially, when these first shocks are not yet strong and the postshock temperatures are rather small, the two postshock temperatures are almost identical. However, it is seen that at greater heights, the temperature for the case with time-dependent ionization is much higher than in the case of time-independent ionization. This can be attributed to the high-energy loss that in the time-independent case is spent to rapidly ionize hydrogen. In the time-dependent case, where few hydrogen atoms get ionized, the thermal energy remains as in an adiabatic wave and thus leads to high temperature. Note that for subsequent shocks, the differences in postshock properties between models with and without time-dependent ionization become smaller as a result of the fact that the mean temperature and density structures of the atmospheres will adjust to different values.

3.5. Frequency Integration Tests

As the radiation field significantly enters the radiative emission and absorption rates, it is important to know how sensitively our results depend on the number of frequency points used in the Lyman continuum. A poorly resolved radiation field can change the temperature amplitude of the
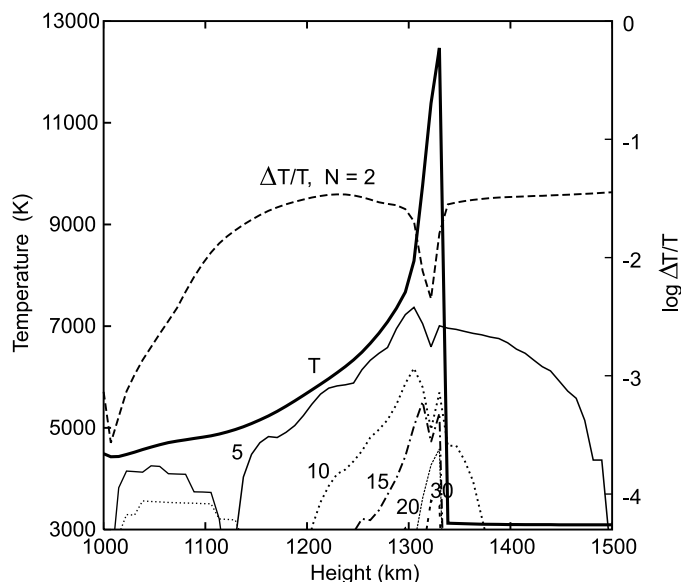
FIG. 5.—Relative temperature differences for a longitudinal MHD tube wave calculation using different numbers of frequency points to cover the Lyman continuum. The test is for the wave phase of Fig. 3e. Also shown is the temperature of that phase.

FIG. 6.—Accuracy of the evaluation of the radiative absorption rate R_{13} when using different numbers of interpolation points for the frequency integration. The test is for the wave phase of Fig. 3e. Also shown is the temperature of that phase.

wave and also significantly the radiative absorption rate R_{13}. In our calculations, the wavelength regime for the Lyman continuum is taken between 913 and 521 Å. For the frequency test, we vary the number of frequency points in this interval from merely two points to 40 points. The results obtained with 40 frequency points are regarded as sufficiently accurate.

In Figure 5 we have taken a wave phase $t = 12$ s before the phase shown in Figure 3e and made several continuations of the wave calculation over about 25 additional time steps until reaching the phase of Figure 3e. For each continuation we took another set of frequency points to cover the Lyman continuum. Comparing the temperatures of the resulting wave phases relative to these obtained with 40 frequency points, we find that in order to have reasonable accuracy we should take at least 15 frequency points. Our calculations in the present paper were based on this value. Figure 5 shows only the part of the atmosphere with the strong shock, which exhibits the largest changes of $\Delta T/T$ for the different test cases.

Note that in the case of time-dependent ionization, a comparison of the temperatures after execution of merely one time step does not constitute a suitable test. The reason is that the radiative field reacts only very slowly to changes imposed by alterations of the radiative transfer treatment. Therefore, it is more appropriate to calculate a larger number of time steps and then assess the difference of the relevant quantities.

Another interesting result of this test is the amount of CPU time needed. This time scales in no way linearly with the number of frequency points. The calculation with 40 points needs nearly 40% more CPU time than the calculation with 10 points, but the calculation with only five points needs the same time as a 10 point case. This is explained by the strong increase of the number of overall iterations when the radiation field is poorly resolved.

Another test is the frequency integration of the Lyman continuum necessary in the absorption rate R_{13}. Interpolat-

ing the Lyman continuum available at the 15 frequency points, we perform the frequency integral in R_{13}. Figure 6 shows such a test for the wave phase of Figure 3e. Shown is the temperature distribution and the relative deviations $\Delta R_{13}/R_{13}$ for different numbers of frequency points used for the computation of the radiative rates. The total number of frequency points, obtained through interpolation, varies between 15 and 100. In the case of 100 points, the rates R_{13} are considered to be exact and are used for comparison with R_{13} rates found for a lower number of frequencies. It is seen that to use the 15 frequency points for which the Lyman continuum is provided gives R_{13} with relatively poor accuracy. We therefore decided to use an interpolation with 100 frequency points to evaluate this absorption rate in all our calculations. Note that the increase of the frequency points for the calculation of the radiative rates increases the required CPU time by only 15%.
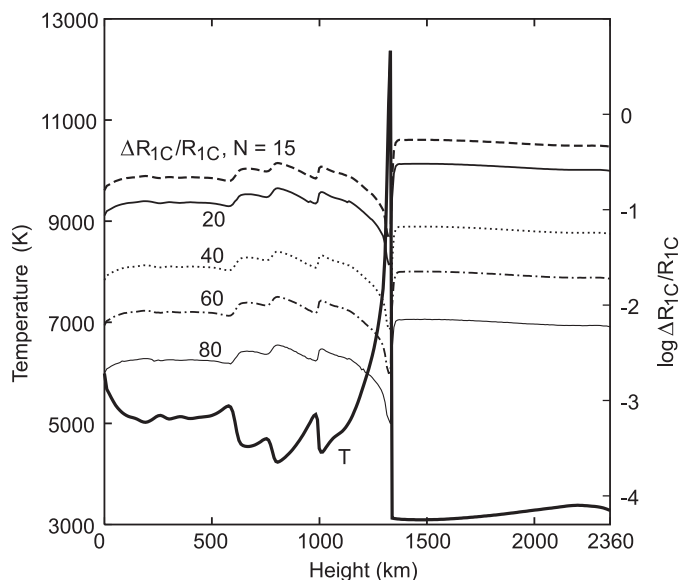
3.6. Height Grid Tests

To see how our calculations depend on the selected number of height points N, we have performed wave computations with $N = 79$, 128, 256, and 500 height points. As mentioned above, there are additional shock points that the code introduces automatically whenever shocks form. Therefore, the four phases shown in Figure 7 have the same number of shocks. For this test we selected monochromatic waves because here the shock formation was similar in the four computations and resulted in temperature distributions only slightly different from the phase with $N = 256$ points shown in Figure 7. The small differences in the shock positions are seen in the distribution of the slight postshock bumps of the H^+/H distributions near 1000 and 1500 km height. In stochastic wave computations, as a result of the shock overtakings, much more disparate temperature distributions would be found. Recalling that in our wave computations we use a standard value of $N = 256$ points, it is seen in Figure 7 that taking 128 or 79 points would decrease the accuracy of the ionization treatment considerably.
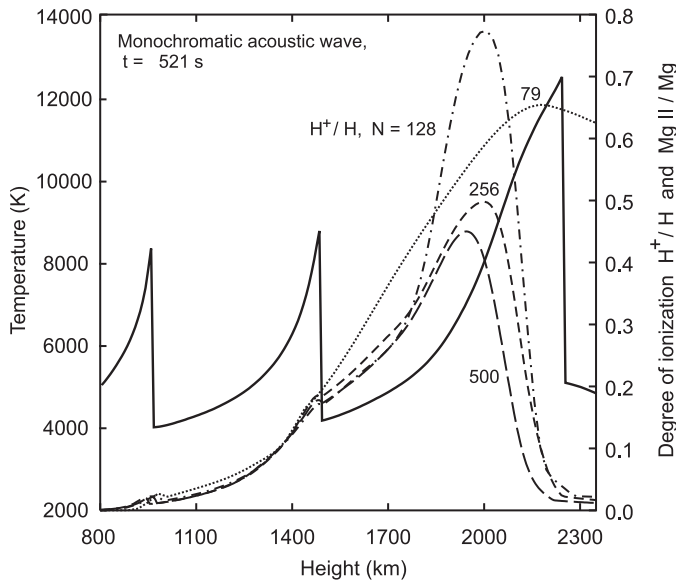
FIG. 7.—Degree of hydrogen ionization in wave calculations with different numbers of height points N. All wave phases are shown at time $t = 521$ s. The wave phase with $N = 256$ height points is also shown in Fig. 2b. Also displayed is the temperature for that phase.

However, to double the number of height points would only marginally increase the accuracy. Here it has to be noted that the difference seen in Figure 7 for the four computations is especially large because the calculations are still close to the start of the computations. At later times, when a permanently rising mean H^+/H distribution is established, one expects that the ionization treatment will depend only very little on the choice of the number of height points N.

3.7. The Λ-Iteration

As mentioned above, there is the problem that both the level populations and the radiation fields are unknown and that in a correct solution one must have a consistent set of
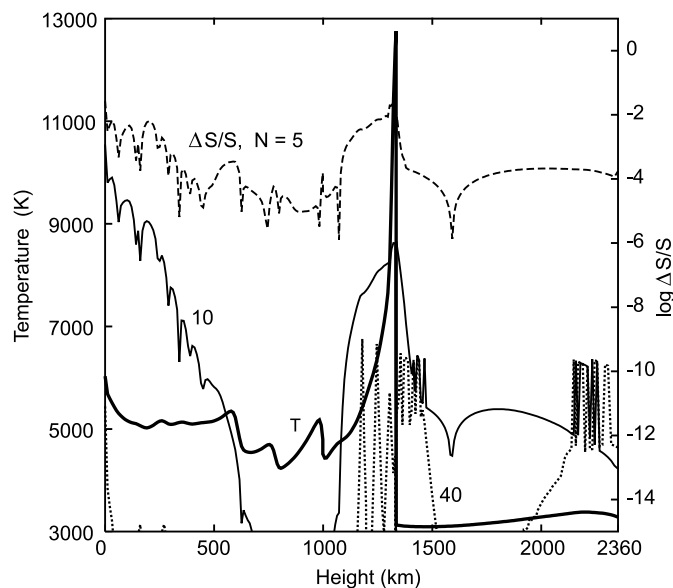
FIG. 8.—Changes in the Lyman edge source function $\Delta S_\nu/S_\nu$ after different numbers of Λ-iterations for the wave phase of Fig. 3e. Also shown is the temperature of that phase.
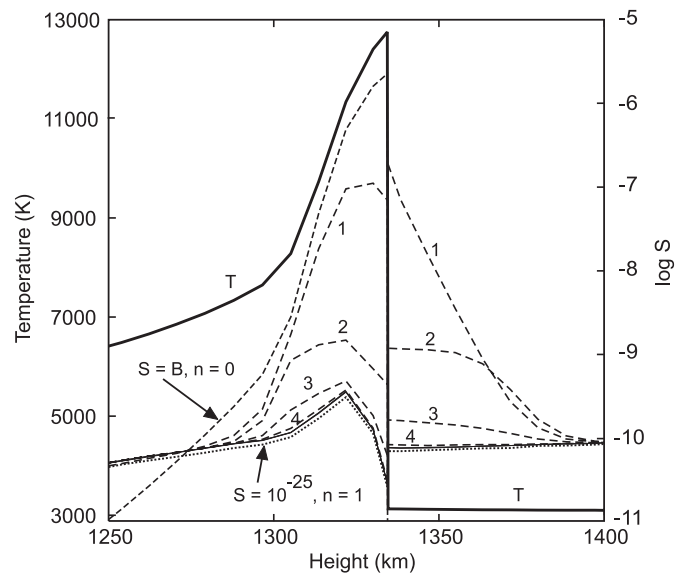
FIG. 9.—Convergence of the Lyman edge source function S_ν during Λ-iteration starting from initial assumed source functions for the wave phase of Fig. 3e. Also shown is the temperature of that phase.

both types of quantities. In our present work we use the Λ-iteration for the treatment of the Lyman continuum, which normally (for lines) is well known (e.g., Ulmschneider 1994) to converge rather slowly. Detailed numerical tests, however, convinced us that the Λ-iteration is a viable method for our wave calculations. In Figure 8 the phase of Figure 3e is used to show the changes that result when larger numbers of Λ-iterations are made. Displayed is the change $\Delta S/S$ relative to the source function S_ν at the Lyman edge (essentially the ratio n_3/n_1) obtained for a very large number of Λ-iterations. It is seen that after already 40 iterations we have essentially reached machine accuracy.

That Λ-iterations in our wave calculations lead to the correct source function can be also seen in Figure 9, where we have started the Λ-iteration using very different initial source functions. Figure 9 shows (dashed lines) for the wave phase of Figure 3e how the Λ-iteration lets the source function converge from above to a final value when we start originally with a Planck function $S_\nu = B_\nu$. That this final state is not a bad metastable state where the convergence becomes exceedingly slow is seen from our second set of calculations (dotted lines) where we started from a source function that was essentially zero, $S_\nu = 1 \times 10^{-13}$. Here the convergence approaches the final solution from below. It is interesting that the latter approach converges much more rapidly than the case with $S_\nu = B_\nu$.

4. CONCLUSIONS

A new numerical method is presented to compute the propagation of acoustic and longitudinal MHD tube waves in stellar atmospheres together with the treatment of time-dependent hydrogen ionization and the NLTE radiation losses of various lines and continua. For an $N = 3$ level hydrogen atom the time-dependent rate equations and the hydrodynamic or MHD equations are solved in a consistent manner with the radiative transfer. The system of equations for the particle conservations could be reduced to the solution of a fifth-order polynomial for the electron density that

has only one physically acceptable solution. This could be generalized to atomic models with an arbitrary number of N levels, where one has $N - 1$ bound levels plus the continuum level. We found that for an N-level atom one will obtain an $N + 2$ level polynomial for the electron density.

Applying the method to monochromatic and stochastic acoustic wave calculations and a longitudinal stochastic MHD tube wave calculation, the following results were obtained:

1. In a monochromatic wave calculation with the time-dependent hydrogen and Mg ionization treatment we find that the wave leads to permanent increase of the degree of hydrogen and Mg II ionization with height and that the temperature fluctuations of the (shock) wave are largely uncoupled from the degree of ionization.

2. This is very different compared to the case in which the hydrogen ionization is treated using a time-independent approach, where the statistical rate equations are solved. In that case it is found that the degree of ionization is strongly correlated with the temperature amplitude of the wave.

3. In stochastic acoustic wave calculations strong shocks appear periodically with roughly a 3 minute period. In the very hot postshock regions of these shocks the degree of ionization is high and correlated to the temperature. This behavior is similar to what has been found by Carlsson & Stein (1997, 2002).

4. Longitudinal MHD tube waves behave very similar to acoustic waves.

5. Various tests on the number of frequency and height points, as well as on the rate of convergence of the Λ-iteration, show that the present method appears to be reasonably accurate and reliable.

6. As mentioned in § 1, it is presently not possible, as a result of inadequate computational power, to perform a full three-dimensional simulation of a chromospheric acoustic shock wave field that includes the time-dependent hydrogen ionization and is generated by a finite set of acoustic sources at discrete locations distributed over the solar surface. We suggest that the best avenue to progress toward more realistic theoretical solar chromosphere models might therefore be to use monochromatic plane wave computations. Such computations represent fairly well the weak acoustic shock heating due to many different waves propagating in spherical or cone geometries, which superpose one another and intersect at oblique angles. Such computations would avoid shock overtakings, which generate strong solitary shocks that typically occur as a peculiarity of plane wave computations using acoustic spectra.

APPENDIX A

PARTICLE EQUATIONS AND THERMODYNAMIC DERIVATIVES

We assume a gas of astrophysical composition consisting of hydrogen, helium, and metals with the abundances X_{el}, Y_{el}, and Z_{el}, respectively, and $X_{\text{el}} + Y_{\text{el}} + Z_{\text{el}} = 1$. For our models we assume $X_{\text{el}} = 0.9$ and $Z_{\text{el}} = 10^{-4} X_{\text{el}}$. Hydrogen is assumed to be partially ionized, helium is neutral, and the (representative) metal is singly ionized. This is an appropriate assumption for most stellar photospheres, chromospheres, and transition regions. In stellar chromospheres and transition regions, the ionization degree of the metals increases as a function of height, but most of the electrons are supplied by the much more abundant hydrogen. With the neutral hydrogen density $n_{\text{H}} = n_1 + n_2$, the proton density $n_{\text{H}^+} = n_3$, the neutral helium density n_{He}, the singly ionized metal density n_{M^+}, and the heavy particle density n_A, we find

$$n_{\text{H}} + n_{\text{H}^+} = n_1 + n_2 + n_3 = n_A X_{\text{el}} , \tag{A1}$$

$$n_{\text{He}} = n_A Y_{\text{el}} , \tag{A2}$$

$$n_{M^+} = n_A Z_{\text{el}} . \tag{A3}$$

The heavy particle density is then given by

$$n_A = n_{\text{H}} + n_{\text{H}^+} + n_{\text{He}} + n_{M^+} = \frac{n_{\text{H}} + n_{\text{H}^+}}{X_{\text{el}}} , \tag{A4}$$

while for the electron density we get

$$n_e = n_{\text{H}^+} + n_{M^+} = n_{\text{H}^+} + (n_{\text{H}} + n_{\text{H}^+}) \frac{Z_{\text{el}}}{X_{\text{el}}} . \tag{A5}$$

The total particle density by number is then given by

$$n_{\text{tot}} = \frac{p}{kT} = n_A + n_e = (n_{\text{H}} + n_{\text{H}^+}) \frac{1 + Z_{\text{el}}}{X_{\text{el}}} + n_{\text{H}^+} , \tag{A6}$$

where p and T are gas pressure and temperature, respectively, and k is the Boltzmann constant.

Let us now discuss the thermodynamic variables and derivatives. Only affected by the presence of heavy particles, the density is given by

$$\rho = m_A n_A = m_A(n_{\text{tot}} - n_e) = m_A\left(\frac{p}{kT} - n_e\right) , \tag{A7}$$

where the average mass of a particle is given by

$$m_A = (1.008 X_{\text{el}} + 4.003 Y_{\text{el}} + 16 Z_{\text{el}})m_H . \tag{A8}$$

Here $m_H = k/\Re$ is the atomic mass unit and $\Re$ the gas constant. For the thermodynamic derivatives one obtains

$$\left(\frac{\partial\rho}{\partial p}\right)_T = m_A\left(\frac{\partial n_A}{\partial p}\right)_T = m_A\left(\frac{\partial n_{\text{tot}}}{\partial p}\right)_T - m_A\left(\frac{\partial n_e}{\partial p}\right)_T = \frac{m_A}{kT} - m_A\left(\frac{\partial n_e}{\partial p}\right)_T , \tag{A9}$$

$$\left(\frac{\partial\rho}{\partial T}\right)_p = m_A\left(\frac{\partial n_A}{\partial T}\right)_p = \frac{m_A n_{\text{tot}}}{kT} - m_A\left(\frac{\partial n_e}{\partial T}\right)_p . \tag{A10}$$

The internal energy E per gram is given by

$$E = \frac{(3/2)p + n_{H^+}E_H}{\rho} , \tag{A11}$$

where E_H is the ionization energy of hydrogen and where from equations (A3)–(A5) one has

$$n_{H^+} = n_e - n_A Z_{\text{el}} = n_e - (n_{\text{tot}} - n_e)Z_{\text{el}} = n_e(1 + Z_{\text{el}}) - n_{\text{tot}}Z_{\text{el}} , \tag{A12}$$

which leads to

$$\left(\frac{\partial E}{\partial T}\right)_p = -\frac{E}{\rho}\left(\frac{\partial\rho}{\partial T}\right)_p + \frac{E_H}{\rho}\left[(1 + Z_{\text{el}})\left(\frac{\partial n_e}{\partial T}\right)_p + Z_{\text{el}}\frac{n_{\text{tot}}}{T}\right] . \tag{A13}$$

The entropy S per gram is given by

$$S = k\left\{\frac{3}{2}n_{\text{tot}}\ln T + \frac{5}{2}n_{\text{tot}} + (n_1 + n_2)\ln\left[\left(\frac{2\pi m_H k}{h^2}\right)^{3/2}\left(\frac{2}{n_1 + n_2}\right)\right] + n_{H^+}\ln\left[\left(\frac{2\pi m_H k}{h^2}\right)^{3/2}\left(\frac{1}{n_{H^+}}\right)\right]\right.$$

$$\left. + n_{\text{He}}\ln\left[\left(\frac{2\pi m_{\text{He}}k}{h^2}\right)^{3/2}\left(\frac{1}{n_{\text{He}}}\right)\right] + n_e\ln\left[\left(\frac{2\pi m_e k}{h^2}\right)^{3/2}\left(\frac{2}{n_e}\right)\right] + n_{M^+}\ln\left[\left(\frac{2\pi m_M k}{h^2}\right)^{3/2}\left(\frac{2}{n_{M^+}}\right)\right]\right\}\Big/\rho , \tag{A14}$$

where m_{He} and m_M are the atomic mass of helium and the representative metal, respectively. Taking the partial derivative $(\partial/\partial T)_p$ of the combined first and second laws of thermodynamics, $T\,dS = dE - p\,d\rho/\rho^2$, one obtains

$$\left(\frac{\partial T}{\partial S}\right)_p = T\left[\left(\frac{\partial E}{\partial T}\right)_p - \frac{p}{\rho^2}\left(\frac{\partial\rho}{\partial T}\right)_p\right]^{-1} . \tag{A15}$$

As the enthalpy $H = E + p/\rho$ is a thermodynamic variable, $dH = dE + dp/\rho - p\,d\rho/\rho^2 = T\,dS + dp/\rho$ is an exact differential implying $\partial^2 H/\partial p\partial S = \partial^2 H/\partial S\partial p$. This allows us to derive the Maxwell relation

$$\left(\frac{\partial\rho}{\partial S}\right)_p = -\rho^2\left(\frac{\partial T}{\partial p}\right)_S , \tag{A16}$$

where because of

$$\left(\frac{\partial S}{\partial\rho}\right)_p = \left(\frac{\partial S}{\partial T}\right)_p\left(\frac{\partial T}{\partial\rho}\right)_p , \tag{A17}$$

and with equations (A15) and (A16), one has

$$\left(\frac{\partial T}{\partial p}\right)_S = -\frac{T}{\rho^2}\left(\frac{\partial\rho}{\partial T}\right)_p\left[\left(\frac{\partial E}{\partial T}\right)_p - \frac{p}{\rho^2}\left(\frac{\partial\rho}{\partial T}\right)_p\right]^{-1} . \tag{A18}$$

The adiabatic sound speed is given by

$$c_S = \left[\left(\frac{\partial p}{\partial\rho}\right)_S\right]^{1/2} = \left[\left(\frac{\partial\rho}{\partial p}\right)_T + \left(\frac{\partial\rho}{\partial T}\right)_p\left(\frac{\partial T}{\partial p}\right)_S\right]^{-1/2} , \tag{A19}$$

and the mean molecular weight by

$$\mu = \frac{\rho \Re T}{p} \ . \tag{A20}$$

Note that equations (A15)–(A19) can be computed using equations (A9), (A10), and (A13), provided that $(\partial n_e / \partial T)_p$ and $(\partial n_e / \partial p)_T$ are given. In the case of time-dependent NLTE, this requires the solution of the time-dependent statistical rate equations and of the polynomial equation for the electron density n_e (see § 2.6 and Appendix B).

APPENDIX B

SOLUTION OF THE TIME-DEPENDENT RATE EQUATIONS

Note that the following equations have been derived using the Maple V mathematics package, which allows a direct TEX output and thus should be free of typing errors. In a first step, the rate equations (58)–(60) are written as difference equations:

$$\frac{n_{1P} - n_{1T}}{\Delta t} = \frac{1}{2} [n_2 P_{21} + n_3 P_{31} - n_1 (P_{12} + P_{13} + W)]_P + \frac{1}{2} \underbrace{[n_2 P_{21} + n_3 P_{31} - n_1 (P_{12} + P_{13} + W)]_T}_{k_1} , \tag{B1}$$

$$\frac{n_{2P} - n_{2T}}{\Delta t} = \frac{1}{2} [n_1 P_{12} + n_3 P_{32} - n_2 (P_{21} + P_{23} + W)]_P + \frac{1}{2} \underbrace{[n_1 P_{12} + n_3 P_{32} - n_2 (P_{21} + P_{23} + W)]_T}_{k_2} , \tag{B2}$$

$$\frac{n_{3P} - n_{3T}}{\Delta t} = \frac{1}{2} [n_1 P_{13} + n_2 P_{23} - n_3 (P_{31} + P_{32} + W)]_P + \frac{1}{2} \underbrace{[n_1 P_{13} + n_2 P_{23} - n_3 (P_{31} + P_{32} + W)]_T}_{k_3} \ . \tag{B3}$$

The subscript P marks the values at (height) grid point P, for which the values n_i are unknown, and subscript T denotes the values at the footpoint of the (fluid path) C^0 characteristic going through P. The values at T are all known from the last time step. We find that equations (B1)–(B3) can be written as an inhomogeneous linear system,

$$a_1 n_1 - b_1 n_2 - c_1 n_3 = G_1 , \tag{B4}$$

$$a_2 n_1 - b_2 n_2 + c_2 n_3 = -G_2 , \tag{B5}$$

$$a_3 n_1 + b_3 n_2 + c_3 n_3 = G_3 , \tag{B6}$$

with

$$a_1 = -\left(n_e \Omega_{21} e^{-E_{12}/kT} + R_{13} + n_e \Omega_1 e^{-E_1/kT} + W + \frac{2}{\Delta t} \right) , \tag{B7a}$$

$$b_1 = -\left(\frac{A_{21}}{1 + \tau_{\mathrm{Ly}}} + n_e \frac{\Omega_{21}}{4} \right) , \tag{B7b}$$

$$c_1 = -\left(n_e \tilde{R}_{31} + n_e^2 g_1 \Omega_1 \right) , \tag{B7c}$$

$$a_2 = -\left(n_e \Omega_{21} e^{-E_{12}/kT} \right) , \tag{B7d}$$

$$b_2 = -\left(\frac{A_{21}}{1 + \tau_{\mathrm{Ly}}} + n_e \frac{\Omega_{21}}{4} + R_{23} + n_e \Omega_2 e^{-E_2/kT} + W + \frac{2}{\Delta t} \right) , \tag{B7e}$$

$$c_2 = -\left(n_e \tilde{R}_{32} + n_e^2 g_2 \Omega_2 \right) , \tag{B7f}$$

$$a_3 = R_{13} + n_e \Omega_1 e^{-E_1/kT} , \tag{B7g}$$

$$b_3 = R_{23} + n_e \Omega_2 e^{-E_1/4kT} , \tag{B7h}$$

$$c_3 = -\left(n_e \tilde{R}_{31} + n_e^2 g_1 \Omega_1 + n_e \tilde{R}_{32} + n_e^2 g_2 \Omega_2 + W + \frac{2}{\Delta t} \right) , \tag{B7i}$$

$$G_1 = -\frac{2 n_{1T}}{\Delta t} - k_1 , \tag{B7j}$$

$$G_2 = -\frac{2 n_{2T}}{\Delta t} - k_2 , \tag{B7k}$$

$$G_3 = -\frac{2 n_{3T}}{\Delta t} - k_3 , \tag{B7l}$$

where we have used the definitions of § 2.6. From this the formal solution of equations (B4)–(B6) is easily found:

$$n_1 = \frac{-G_2 b_3 c_1 + G_1 b_3 c_2 + G_2 b_1 c_3 + G_1 b_2 c_3 + G_3 b_1 c_2 + G_3 b_2 c_1}{DN} , \tag{B8}$$

$$n_2 = \frac{G_3 a_2 c_1 + G_1 a_2 c_3 + G_2 a_1 c_3 + G_3 a_1 c_2 + G_2 a_3 c_1 - G_1 a_3 c_2}{DN} , \tag{B9}$$

$$n_3 = \frac{-G_2 a_1 b_3 - G_3 a_2 b_1 - G_2 a_3 b_1 + G_3 a_1 b_2 - G_1 a_2 b_3 - G_1 a_3 b_2}{DN} , \tag{B10}$$

with

$$DN = a_1 b_3 c_2 - a_2 b_1 c_3 + a_3 b_1 c_2 + a_1 b_2 c_3 + a_2 b_3 c_1 + a_3 b_2 c_1. \tag{B11}$$

From equation (B7) it is seen that the coefficients of this solution depend on the unknown value of n_e. We therefore rewrite the coefficients by separating the electron density:

$$a_1 = \alpha_1 + n_e \alpha_2, \qquad \alpha_1 = -R_{13} - \frac{2}{\Delta t} - W, \qquad \alpha_2 = -\Omega_{21} e^{-E_{12}/kT} - \Omega_1 e^{-E_1/kT} , \tag{B12a}$$

$$b_1 = \beta_1 + \beta_2 n_e, \qquad \beta_1 = -\frac{A_{21}}{1 + \tau_{\mathrm{Ly}}}, \qquad \beta_2 = -\frac{\Omega_{21}}{4} , \tag{B12b}$$

$$c_1 = \gamma_1 n_e + \gamma_2 n_e^2, \qquad \gamma_1 = -\tilde{R}_{31}, \qquad \gamma_2 = -g_1 \Omega_1 , \tag{B12c}$$

$$a_2 = \alpha_3 n_e, \qquad \alpha_3 = -\Omega_{21} e^{-E_{12}/kT}, \tag{B12d}$$

$$b_2 = \beta_3 + \beta_4 n_e, \qquad \beta_3 = -\frac{A_{21}}{1 + \tau_{\mathrm{Ly}}} - R_{23} - \frac{2}{\Delta t} - W, \qquad \beta_4 = -\frac{\Omega_{21}}{4} - \Omega_2 e^{-E_2/kT} , \tag{B12e}$$

$$c_2 = \gamma_3 n_e + \gamma_4 n_e^2, \qquad \gamma_3 = -\tilde{R}_{32}, \qquad \gamma_4 = -g_2 \Omega_2 \tag{B12f}$$

$$a_3 = \alpha_4 + \alpha_5 n_e, \qquad \alpha_4 = R_{13} \quad \alpha_5 = \Omega_1 e^{-E_1/kT} , \tag{B12g}$$

$$b_3 = \beta_5 + \beta_6 n_e, \qquad \beta_5 = R_{23}, \qquad \beta_6 = \Omega_2 e^{-E_1/4kT} , \tag{B12h}$$

$$c_3 = \gamma_5 + \gamma_6 n_e + \gamma_7 n_e^2, \qquad \gamma_5 = -\left(W + \frac{2}{\Delta t}\right), \qquad \gamma_6 = -(\tilde{R}_{31} + \tilde{R}_{32}), \qquad \gamma_7 = -(g_1 \Omega_1 + g_2 \Omega_2) . \tag{B12i}$$

The electron density n_e and the occupation numbers n_i are connected via equation (62),

$$n_e = n_3 + (n_1 + n_2 + n_3)\frac{Z_{\mathrm{el}}}{X_{\mathrm{el}}} . \tag{B13}$$

We substitute equations (B8)–(B10) into equation (B13) using the expressions given by equation (B12) for the coefficients a_i, b_i, and c_i and obtain an equation only for n_e. After some algebra we obtain the polynomial equation (80) already mentioned in § 2.6:

$$v_5 n_e^5 + v_4 n_e^4 + v_3 n_e^3 + v_2 n_e^2 + v_1 n_e + v_0 = 0 , \tag{B14}$$

with the coefficients

$$v_5 = (\beta_2 \gamma_4 + \gamma_2 \beta_4)\alpha_5 + (\alpha_2 \gamma_4 + \alpha_3 \gamma_2)\beta_6 + \alpha_2 \gamma_7 \beta_4 - \alpha_3 \beta_2 \gamma_7 , \tag{B15a}$$

$$v_4 = (-\beta_1 \gamma_7 + \gamma_2 \beta_5 - \beta_2 \gamma_6 + \gamma_1 \beta_6)\alpha_3 + (\gamma_2 \alpha_4 + \alpha_1 \gamma_7 + \gamma_1 \alpha_5 + \alpha_2 \gamma_6)\beta_4 + (\alpha_2 \beta_5 + \alpha_5 \beta_1 + \alpha_1 \beta_6 + \alpha_4 \beta_2)\gamma_4$$
$$+ \alpha_2 \beta_6 \gamma_3 + \gamma_2 \alpha_5 \beta_3 + \alpha_5 \beta_2 \gamma_3 + \alpha_2 \gamma_7 \beta_3 , \tag{B15b}$$

$$v_3 = \frac{[(-G_3 \gamma_2 - G_1 \gamma_7)\alpha_3 + (-\alpha_2 \gamma_7 - \beta_2 \gamma_7 - \gamma_2 \alpha_5 + \gamma_2 \beta_6)G_2 - G_3 \beta_2 \gamma_4 + G_1 \gamma_4 \alpha_5 - G_3 \alpha_2 \gamma_4 - G_1 \gamma_4 \beta_6 - G_1 \gamma_7 \beta_4 - G_3 \gamma_2 \beta_4]Z_{\mathrm{el}}}{X_{\mathrm{el}}}$$
$$+ (\gamma_6 \beta_4 + \beta_5 \gamma_4 + \beta_6 \gamma_3 + \gamma_7 \beta_3)\alpha_1 + (-\beta_1 \gamma_6 - \beta_2 \gamma_5 + \gamma_1 \beta_5)\alpha_3 + (\gamma_1 \beta_4 + \beta_1 \gamma_4 + \beta_2 \gamma_3 + \gamma_2 \beta_3)\alpha_4 + \alpha_2 \gamma_6 \beta_3 + \gamma_1 \alpha_5 \beta_3$$
$$+ \alpha_5 \beta_1 \gamma_3 + \alpha_2 \gamma_5 \beta_4 + \alpha_2 \beta_5 \gamma_3 , \tag{B15c}$$

$$v_2 = [(G_1 \beta_6 + G_3 \beta_2 - G_3 \gamma_1 - G_1 \gamma_6)\alpha_3 + (-G_3 \gamma_2 - G_1 \gamma_7)\beta_3 + (-G_3 \alpha_2 + G_1 \alpha_5 - G_3 \gamma_1 - G_1 \gamma_6)\beta_4$$
$$+ (-G_1 \beta_5 - G_3 \beta_1 - G_3 \alpha_1 + G_1 \alpha_4)\gamma_4 - G_2 \beta_2 \gamma_6 - G_2 \beta_1 \gamma_7 + (G_2 \alpha_2 - G_1 \gamma_3 + G_2 \gamma_1)\beta_6 - G_2 \alpha_1 \gamma_7 - G_2 \alpha_2 \gamma_6$$
$$+ G_2 \alpha_5 \beta_2 - G_2 \gamma_2 \alpha_4 + G_2 \gamma_2 \beta_5 - G_3 \alpha_2 \gamma_3 + G_1 \gamma_3 \alpha_5 - G_3 \beta_2 \gamma_3 - G_2 \gamma_1 \alpha_5]Z_{\mathrm{el}}/X_{\mathrm{el}} + (G_1 \beta_6 - \beta_1 \gamma_5 + G_3 \beta_2)\alpha_3$$
$$+ (\gamma_1 \alpha_4 + \alpha_2 \gamma_5 + \alpha_1 \gamma_6)\beta_3 + (G_1 \alpha_5 - G_3 \alpha_2 + \alpha_1 \gamma_5)\beta_4 + G_2 \alpha_2 \beta_6 + G_2 \alpha_5 \beta_2 + \alpha_4 \beta_1 \gamma_3 + \alpha_1 \beta_5 \gamma_3 , \tag{B15d}$$

$$v_1 = [(-G_3\alpha_2 + G_1\alpha_5 - G_3\gamma_1 - G_1\gamma_6)\beta_3 + (-G_1\gamma_5 - G_3\alpha_1 + G_1\alpha_4)\beta_4 + (-G_1\beta_5 - G_3\beta_1 - G_3\alpha_1 + G_1\alpha_4)\gamma_3$$
$$+ (G_1\alpha_3 + G_2\alpha_2 + G_2\gamma_1)\beta_5 - G_2\alpha_1\gamma_6 + (-G_1\alpha_3 - G_2\alpha_2 - G_2\beta_2)\gamma_5 + \alpha_3 G_3\beta_1 + G_2\alpha_4\beta_2 - G_2\gamma_1\alpha_4 - G_2\beta_1\gamma_6 + G_2\alpha_1\beta_6$$
$$+ G_2\alpha_5\beta_1]Z_{el}/X_{el} + (G_1\alpha_5 - G_3\alpha_2 + \alpha_1\gamma_5)\beta_3 + (G_1\alpha_4 - G_3\alpha_1)\beta_4 + (G_1\alpha_3 + G_2\alpha_2)\beta_5 + G_2\alpha_5\beta_1 + G_2\alpha_1\beta_6$$
$$+ G_2\alpha_4\beta_2 + \alpha_3 G_3\beta_1 ,\tag{B15e}$$

$$v_0 = \frac{[(-G_1\gamma_5 - G_3\alpha_1 + G_1\alpha_4)\beta_3 + (-\beta_1\gamma_5 + \alpha_4\beta_1 + \alpha_1\beta_5 - \alpha_1\gamma_5)G_2]Z_{el}}{X_{el}} + (G_1\alpha_4 - G_3\alpha_1)\beta_3 + (\alpha_1\beta_5 + \alpha_4\beta_1)G_2 ,\tag{B15f}$$

APPENDIX C

SOLUTIONS FOR AN N-LEVEL ATOM

We now discuss the generalized case of a hydrogen atom consisting of N levels, $N - 1$ bound levels plus the continuum level. In this case, the electron density is obtained as the solution of a polynomial equation of the order of $N + 2$. This can be shown as follows. In the general case we start from a set of N equations such as equations (B4)–(B6), which gives us an $N \times N$ coefficient matrix. In this matrix all coefficients depend either linearly or quadratically on n_e (or show no explicit dependence on n_e such as all bound-bound radiative rates). The coefficients with n_e^2 occur only in the last column because they appear only in the collision rates between continuum and bound levels. The solution of the set of equations using Gaussian elimination leads to expressions of the form

$$n_j = \frac{T_{11} + T_{12} + T_{13} + \dots}{T_{21} + T_{22} + T_{23} + \dots} ,\tag{C1}$$

where

$$T_{1j} = \prod_{k=1}^{N} f_k , \qquad T_{2j} = \prod_{k=1}^{N} g_k ,\tag{C2}$$

and the f_k and g_k are elements of the coefficient matrix. All products T_{1j} and T_{2j} are of the nature that none of their factors originate from the same row or column. The highest exponent in n_e of the T_{1j} and T_{2j} can thus be calculated as follows. The n_e^2 terms appear only in the Nth column. In all other $N - 1$ columns, the electron density appears at most linearly. The maximum possible n_e exponent appearing in the products T_{1j} and T_{2j} is thus given by $n_e^{N-1} n_e^2 = n_e^{N+1}$. Moreover, for a hydrogen atom with N levels one also obtains an equation for the electron density similar to equation (B13), which relates the electron density to the total number density of the bound levels n_j via

$$n_e = \sum_{j=1}^{N} h_j n_j ,\tag{C3}$$

where the h_j depend only on X_{el} and Z_{el}. Introducing equation (C1) in equation (C3) and multiplying with the main denominator, we obtain a polynomial of the order of $N + 2$.

REFERENCES

Ayres, T. R. 1975, Ph.D. thesis, Univ. Colorado
Buchholz, B., Hauschildt, P., Rammacher, W., & Ulmschneider, P. 1994, A&A, 285, 987
Buchholz, B., Ulmschneider, P., & Cuntz, M. 1998, ApJ, 494, 700
Burke, P. G., Ormonde, S., & Whittaker, W. 1967, Proc. Phys. Soc. London, 92, 319
Carlsson, M. 1986, A Computer Program for Solving Multi-Level Non-LTE Radiative Transfer Problems in Moving or Static Atmospheres, Uppsala Astron. Obs. Rep. 33
Carlsson, M., Judge, P. G., & Wilhelm, K. 1997, ApJ, 486, L63
Carlsson, M., & Stein, R. F. 1992, ApJ, 397, L59
———. 1994, in Chromospheric Dynamics, ed. M. Carlsson (Oslo: Inst. Theor. Astrophys.), 47
———. 1997, ApJ, 481, 500
———. 2002, ApJ, 572, 626
Cuntz, M. 1990, ApJ, 353, 255
———. 1999, A&A, 350, 1100
Cuntz, M., Rammacher, W., & Ulmschneider, P. 1994, ApJ, 432, 690
Cuntz, M., & Ulmschneider, P. 1988, A&A, 193, 119
Fawzy, D. E., Rammacher, W., Ulmschneider, P., Musielak, Z. E., & Stepien, K. 2002, A&A, 386, 971
Fawzy, D. E., Ulmschneider, P., & Cuntz, M. 1998, A&A, 336, 1029
Fleck, B., & Deubner, F.-L. 1989, A&A, 224, 245
Hansteen, V. 1993, ApJ, 402, 741
Herbold, G., Ulmschneider, P., Spruit, H. C., & Rosner, R. 1985, A&A, 145, 157
Hünerth, G., & Ulmschneider, P. 1995, A&A, 293, 166

Judge, P. G., Carlsson, M., & Wilhelm, K. 1997, ApJ, 490, L195
Judge, P. G., & Carpenter, K. G. 1998, ApJ, 494, 828
Kalkofen, W. 2001, ApJ, 557, 376
———. 2003, in ASP Conf. Ser. 286, Current Theoretical Models and High Resolution Solar Observations: Preparing for ATST, ed. A. A. Pevtsov & H. Uitenbroek (San Francisco: ASP), 385
Kalkofen, W., & Ulmschneider, P. 1984, in Methods in Radiative Transfer, ed. W. Kalkofen (Cambridge: Cambridge Univ. Press), 131
———. 1999, Curr. Sci., 77, 1497
Kalkofen, W., Ulmschneider, P., & Avrett, E. H. 1999, ApJ, 521, L141
Kalkofen, W., Ulmschneider, P., & Schmitz, F. 1984, ApJ, 287, 952
Klein, R. I., Stein, R. F., & Kalkofen, W. 1976, ApJ, 205, 499
Kneer, F. 1980, A&A, 87, 229
Kneer, F., & Nakagawa, Y. 1976, A&A, 47, 65
Kuperus, M. 1972, Sol. Phys., 22, 257
Landau, L. D., & Lifshitz, E. M. 1959, Fluid Mechanics (London: Pergamon)
Lighthill, M. J. 1978, Waves in Fluids (Cambridge: Cambridge Univ. Press)
Musielak, Z. E., Rosner, R., Gail, H.-P., & Ulmschneider, P. 1995, ApJ, 448, 865
Musielak, Z. E., Rosner, R., Stein, R. F., & Ulmschneider, P. 1994, ApJ, 423, 474
Musielak, Z. E., Rosner, R., & Ulmschneider, P. 1989, ApJ, 337, 470
———. 2000, ApJ, 541, 410
———. 2002, ApJ, 573, 418
Noyes, R. W., & Kalkofen, W. 1970, Sol. Phys., 15, 120
Percival, I. C. 1966, Nucl. Fusion, 6, 182

Rammacher, W., & Ulmschneider, P. 1992, A&A, 253, 586
Skartlien, R., Carlsson, M., & Stein, R. F. 1994, in Chromospheric
    Dynamics, ed. M. Carlsson (Oslo: Inst. Theor. Astrophys.), 79
Sutmann, G., Musielak, Z. E., & Ulmschneider, P. 1998, A&A, 340, 556
Theurer, J. 1998, Ph.D. thesis, Univ. Heidelberg
Ulmschneider, P. 1970, Sol. Phys., 12, 403
———. 1986, A&A, 168, 308
———. 1994, A&A, 288, 1021
———. 2003, in Lectures in Solar Physics, Lecture Notes in Physics, ed.
    H. M. Antia, A. Bhatnagar, & P. Ulmschneider (Berlin: Springer), 234
Ulmschneider, P., & Kalkofen, W. 1978, A&A, 69, 407
Ulmschneider, P., Kalkofen, W., Nowak, T., & Bohn, H. U. 1977, A&A,
    54, 61

Ulmschneider, P., Muchmore, D., & Kalkofen, W. 1987, A&A, 177, 292
Ulmschneider, P., & Musielak, Z. E. 1998, A&A, 338, 311
Ulmschneider, P., Musielak, Z. E., & Fawzy, D. E. 2001, A&A, 374, 662
Ulmschneider, P., Theurer, J., & Musielak, Z. E. 1996, A&A, 315, 212
Ulmschneider, P., Theurer, J., Musielak, Z. E., & Kurucz, R. 1999, A&A,
    347, 243
Vernazza, J. E., Avrett, E. H., & Loeser, R. 1981, ApJS, 45, 635
Wunnenberg, M., Kneer, F., & Hirzberger, J. 2002, A&A, 395, L51
Zeldovich, Ya. B., & Raizer, Yu. P. 1967, Physics of Shock Waves and
    High-Temperature Hydrodynamic Phenomena, Vol. 2 (New York:
    Academic Press)